

Scaling Relations and Topological Quadruple Points in Light-matter Interactions with Anisotropy and Nonlinear Stark Coupling

Zu-Jian Ying^{1,*}

¹*School of Physical Science and Technology, Lanzhou University, Lanzhou 730000, China*

Universality is a common quality in different physical parameters that is rooted in the deep nature of physical systems. Scaling relation is a typical universality for critical phenomena around a quantum phase transition, while topological classification provides another type of universality essentially different from the critical universality. Both classes of universalities can be present in a single-qubit system with light-matter interactions, as exhibiting generally in the fundamental quantum Rabi model with anisotropy not only for linear coupling but also for nonlinear Stark coupling (NSC). In low frequencies different levels of scaling relations are demonstrated, holding for anisotropic or/and NSCs, locally or globally. At finite frequencies such a critical universality breaks down and diversity is dominant. However, common topological feature of the ground state can be extracted from the node number, which yields a topological class of universality amidst the critical diversity. Both conventional and unconventional topological transitions emerge, with their meeting, which never occurs in linear interaction, enabled by the nonlinear coupling to form topological quadruple points which are found to be spin-invariant points. Sensitivity analysis indicates that the NSC can be another approach to manipulate topological transitions in addition to coupling anisotropy.

PACS numbers:

I. INTRODUCTION

In the frontiers of modern quantum physics and quantum technologies, the past decade has seen the great wave evoked by the extraordinary experimental progresses^{1,2} and tremendous theoretical efforts³⁻⁵ on the studies of light-matter interactions. The remarkable realization of the ultra-strong^{1,6-15} and even deep-strong couplings,^{15,16} has opened the gate to a new regime with a rich phenomenology unexpected in weak couplings. On the other hand, the milestone work of D. Braak revealing the integrability³ of the quantum Rabi model (QRM),¹⁷ which is a most fundamental model of light-interactions, has triggered an intensive dialogue between mathematics and physics¹⁸ and leads to a boom of theoretical developments.^{4,5,19-38,40-64} Without mentioning the ubiquitous role of light-matter interaction and its broad relevance to quantum optics, quantum information and quantum computation,^{1,65-68} quantum metrology,³⁶⁻³⁹ condensed matter,^{2,27,28} and relativistic systems,⁶⁹ the explosively-growing investigations have yielded abundant findings in the QRM and its extensions, such as hidden symmetry,⁶¹⁻⁶⁴ various patterns of symmetry breaking,^{26,27,29} few-body quantum phase transitions,^{5,22-29,70} multicriticalities and multiple points,²⁶⁻²⁸ universality classification,^{24,25,27,53} spectral collapse,^{33-35,46,49} photon blockade effect,^{40,41} spectral conical intersections,⁴³ classical-quantum correspondence,⁴² single-qubit conventional and unconventional topological phase transitions,^{27,28} and so forth.

An intriguing phenomenon most relevant in coupling enhancement may be quantum phase transition (QPT).^{5,22-27,70} Generally speaking, QPTs are transitions of ground states (GSs) induced by a variation of some non-thermal parameter.⁷¹ In contrast to thermal fluctuations in classical phase transitions, QPTs are regarded to be driven by quantum fluctuations and traditionally lie in the thermodynamic limit in condensed matter. Interestingly, the QRM as a few-body system also exhibits a QPT^{22,23,25} in the low-frequency limit, i.e., $\omega/\Omega \rightarrow 0$ where ω is the bosonic frequency and Ω is the atomic level splitting or tunneling strength. It was also suggested that whether the transition should be termed quantum or not is a matter of taste by taking the negligible quantum fluctuations in the photon vacuum state into account.⁵³ Nevertheless, when critical universality is a character often born with QPTs as in the condensed matter, it has been shown that the anisotropic QRM manifests a universal scaling relation in the critical exponent that can be really bridged to the thermodynamic limit.²⁴

Opposite to universality is diversity which represents the quality to be diverse or different. With the opposite qualities universality and diversity are apparently antagonists. Unexpectedly, the universality scenarios in the anisotropic QRM demonstrate that they can turn to support each other. Indeed, the afore-mentioned critical universality of scaling relation needs the condition of low frequency limit, while at finite frequencies the universal scaling relation breaks down and the system properties are dominated by diversity. However, amidst the diversity a new universality classification can be found from the topological structure of the GS wave function.²⁷ In fact, such universality-diversity-universality scenarios involve two different kinds of universalities: one is critical

* yingzj@lzu.edu.cn

universality, while the other is topological universality. Note that such scenarios occur in the anisotropic QRM which is linear in the light-matter interaction, one may wonder whether the universalities are simply a special case or hold more generally, e.g., in a nonlinear coupling.

To get more robust universalities we consider the QRM with both anisotropy and the nonlinear Stark coupling in the present work. We consider both the low-frequency limit and the finite-frequency case. In the low-frequency limit we analytically obtain the phase boundaries of QPTs and extract different levels of scaling relations which are valid respectively in various anisotropic couplings or for both anisotropic and nonlinear Stark couplings, locally around transitions or globally for all critical regimes. At finite frequencies, indeed the critical universality collapses and diversity dominates, while topological phase transitions (TPTs) emerge. Both conventional and unconventional TPTs respectively with and without gap closing are present. Their different sensitivities in response to the nonlinear Stark coupling enable the forming of topological quadruple points, while it never occurs in linear interaction. A further analysis by composite phase diagrams with hexaple points reveals that the topological quadruple points are actually spin-invariant points.

The paper is organized as follows. Section II introduces the anisotropic QRM with nonlinear Stark coupling and addresses the symmetry in quadrature representation. In Section III methods are introduced to obtain analytic boundaries of QPTs in the low-frequency limit. Different levels of scaling relations are extracted. Section IV shows the breakdown of the critical universality and arising of diversity at finite frequencies. Section V presents topological classifications at finite frequencies, with findings of topological quadruple points, composite hexaple points and invariant points. Section VI is devoted to mechanism clarifications. Conclusions and discussions are finally given in Section VII.

II. MODEL AND SYMMETRY

The standard QRM has a linear and isotropic interaction, while in experimental setups extended versions of QRM are often applied. Indeed, coupling anisotropy plays an important role in ultrastrong couplings^{6,31} and is highly tunable.⁷² On the other hand, a so-called Stark nonlinear coupling can be added and realized with adjustable amplitude and sign.^{30,73–75} We consider the QRM with both anisotropy and nonlinear Stark coupling as described by the following Hamiltonian

$$H = \omega a^\dagger a + \frac{\Omega}{2} \sigma_x + \chi \omega \hat{n} \sigma_x + H_g, \quad (1)$$

$$H_g = g [(\tilde{\sigma}_- a^\dagger + \tilde{\sigma}_+ a) + \lambda (\tilde{\sigma}_+ a^\dagger + \tilde{\sigma}_- a)]. \quad (2)$$

Here ω is the frequency of a bosonic mode created (annihilated) by a^\dagger (a), while Ω is atomic level splitting in cavity systems or tunneling strength in superconducting

circuit systems with the qubit (spin) represented by the Pauli matrix $\sigma_{x,y,z}$. The linear coupling strength is controlled by g . The anisotropy λ tunes the ratio of the rotating-wave terms and the counter-rotating terms, with $\lambda = 1$ and $\lambda = 0$ retrieving the QRM¹⁷ and the Jaynes-Cummings model (JCM)⁷⁶ respectively. Note we have adopted the spin notation as in ref.⁵², in which $\sigma_z = \pm$ labels two flux states in flux-qubit circuit systems.⁷⁷ In such a spin notation, the spin raising and lowering operators on σ_x basis are expressed by $\tilde{\sigma}^\pm = (\sigma_z \mp i\sigma_y)/2$, while one can recover the conventional form by a spin rotation $\{\sigma_x, \sigma_y, \sigma_z\} \rightarrow \{\sigma_z, -\sigma_y, \sigma_x\}$ around the axis $\vec{x} + \vec{z}$. The χ term denotes the nonlinear Stark coupling with a limitation $|\chi| \leq 1$ beyond which the system energy would be negatively unbound thus unphysical.

It should be noted that neither the anisotropy nor the nonlinear Stark coupling breaks the parity so that the model preserves the parity symmetry, with H commuting with the parity operator $\hat{P} = \sigma_x (-1)^{a^\dagger a}$. The parity symmetry is relevant for symmetry-protected TPTs^{27,28} as in condensed matter,^{78–81} while there is a hidden symmetry breaking of spin reversion or space inversion for the symmetry-breaking QPT in the GS.²⁷

Changing to the quadrature representation by $a^\dagger = (\hat{x} - i\hat{p})/\sqrt{2}$, $a = (\hat{x} + i\hat{p})/\sqrt{2}$ with momentum $\hat{p} = -i\frac{\partial}{\partial x}$ will facilitate our analysis in the effective position space

$$H = \frac{\omega}{2} \hat{p}^2 + v_{\sigma_z}(x) + H_+ \sigma^+ + H_- \sigma^-, \quad (3)$$

$$H_\pm = \frac{(\Omega - \chi\omega)}{2} \mp g_y i \sqrt{2} \hat{p} + \frac{\chi\omega}{2} (\hat{x}^2 + \hat{p}^2). \quad (4)$$

It should be noted here that, differently from $\tilde{\sigma}^\pm$, the spin raising and lowering in $\sigma_x = \sigma^+ + \sigma^-$, $\sigma_y = -i(\sigma_+ - \sigma_-)$ are now on $\sigma_z = \pm$ basis. We have defined $g'_{y,z} = \sqrt{2}g_{y,z}/\omega$ for $g_y = \frac{(1-\lambda)}{2}g$ and $g_z = \frac{(1+\lambda)}{2}g$, thus g'_z is effectively the amplitude of spin-dependent displacement in harmonic potentials $v_{\sigma_z}(x) = \omega(x + g'_z \sigma_z)^2/2 + \varepsilon_0^z$ where $\varepsilon_0^z = -\frac{1}{2}[g_z'^2 + 1]\omega$. In such a representation the Ω term effectively plays the role of spin flipping in the spin σ_z space and the role of tunneling in the effective position space.^{23,52} The g_y term takes the form $\sqrt{2}g_y \hat{p} \sigma_y$ as the Rashba spin-orbit coupling in nanowires^{82–84} or the equal-weight mixture^{85,86} of the linear Dresselhaus ($\hat{p}_x \sigma_y + \hat{p}_y \sigma_x$) and Rashba ($\hat{p}_x \sigma_y - \hat{p}_y \sigma_x$) spin-orbit couplings in condensed matter^{87,88} and cold atomic gases.^{85,86,89}

The Hamiltonian can be rewritten in x - p dual forms

$$H_x = \frac{\omega}{2} [(-i\frac{\partial}{\partial x} + g'_y \sigma_y)^2 + (x + g'_z \sigma_z)^2] + [\frac{(\Omega - \chi\omega)}{2} + \frac{\chi\omega}{2} (\hat{x}^2 + \hat{p}^2)] \sigma_x + \varepsilon_0, \quad (5)$$

$$H_p = \frac{\omega}{2} [(-i\frac{\partial}{\partial p} - g'_z \sigma_z)^2 + (p + g'_y \sigma_y)^2] + [\frac{(\Omega - \chi\omega)}{2} + \frac{\chi\omega}{2} (\hat{x}^2 + \hat{p}^2)] \sigma_x + \varepsilon_0, \quad (6)$$

where $\varepsilon_0 = -\omega(1 + g_z'^2 + g_y'^2)/2$ and $\hat{x} = i\frac{\partial}{\partial p}$. From H_x and H_p one sees that $\lambda > 0$ and $\lambda < 0$ regimes

are symmetric under the spin rotation and transform to momentum space $\{\sigma_x, \sigma_y, \sigma_z\} \rightarrow \{\sigma_x, -\sigma_z, \sigma_y\}$, $x \rightarrow p$, $\lambda \rightarrow -\lambda$.²⁷ Phase transitions in the GS would involve a linear coupling of order as the critical point in the absence of the nonlinear Stark coupling $g_c^\lambda = \frac{2}{1+|\lambda|}g_s$,^{24,27}

with $g_s = \sqrt{\omega\Omega}/2$, in the low frequency limit $\omega/\Omega \rightarrow 0$ or that of a TPT, $g_{T1}^\lambda = \frac{2}{\sqrt{1-\lambda^2}}g_s$,²⁷ at finite frequencies. At low frequencies, the contribution of $v_{\sigma_z}(x)$ and \hat{x}^2 terms are of leading order²⁶ Ω while the g_y term and \hat{p}^2 term are of subdominant orders $(\omega\Omega)^{1/2}$ and ω^1 . Thus, the $\lambda > 0$ regime is x -type in the sense $\langle \hat{x}^2 \rangle$ is more dominant than $\langle \hat{p}^2 \rangle$, with the main characters more conveniently described by H_x . At finite frequencies, the g_y term has some self-cancellation effect due to oscillation as seen later on, while larger amplitudes of g'_z than g'_y still favor an x -type state in $\lambda > 0$ regime. Hereafter, unless specially mentioned, we shall focus on $\lambda > 0$ regime while one has similar results with a p -type state by H_p in the momentum space for $\lambda < 0$ regime.

III. QPTS AND SCALING RELATIONS IN LOW-FREQUENCY LIMIT

We shall first study the low-frequency limit to extract GS phase diagrams and critical scaling relations. We figure out the full phase diagrams numerically by the exact diagonalization,²⁶ while to obtain analytic phase boundaries and find different scaling relations we need some analytic methods. For the latter purpose, we fall back on a semiclassical variational method for $\lambda \neq 0$ and the exact solution at $\lambda = 0$, as described in this section. We will get different levels of scaling relations and eliminate a singular behavior at $\lambda = 0$. The obtained analytic phase boundaries will also provide a reference to fix the invariant points at finite frequencies in next section.

A. Explicit Solution and Energy at $\lambda = 0$

1. General Solution at Any Frequencies

The explicit exact solution is available for the JCM at $\lambda = 0$ in linear coupling,^{76,90} while here we shall address in the presence of the nonlinear Stark coupling. Setting $\lambda = 0$ drops the counter-rotating terms in the Hamiltonian (1) so that the eigenstates only involve at most two bases in the following form

$$\psi_n^{(\pm)} = \left(C_{n\uparrow}^{(\pm)} |n, \uparrow\rangle_{\sigma_x} + C_{n\downarrow}^{(\pm)} |n+1, \downarrow\rangle_{\sigma_x} \right) / N, \quad (7)$$

$$\psi_0 = |0, \downarrow\rangle_{\sigma_x} \quad (8)$$

where \uparrow, \downarrow are spins states of σ_x as labeled by the subscript of the basis. The coefficients on the basis are ex-

PLICITLY given by

$$C_{n\uparrow}^{(\pm)} = e_{\pm} \pm \sqrt{e_{\pm}^2 + (n+1)g^2}, \quad (9)$$

$$C_{n\downarrow}^{(\pm)} = g\sqrt{(n+1)}, \quad (10)$$

where $e_+ = (n + \frac{1-\chi}{2})\omega$ and $e_- = \frac{1}{2}(\Omega - \omega) + (n + \frac{1}{2})\chi\omega$ and $N = C_{n\uparrow}^{(\pm)2} + C_{n\downarrow}^{(\pm)2}$ is the normalization factor. Corresponding to the above states one can get the eigenenergies

$$E_{\text{JC-Stark}}^{(n,\pm)} = e_{\pm} \pm \sqrt{e_{\pm}^2 + (n+1)g^2}, \quad (11)$$

$$E_{\text{JC-Stark}}^0 = -\frac{\Omega}{2}, \quad (12)$$

respectively. Note the energy in branch $E_{\text{JC-Stark}}^{(n,+)}$ is higher than $E_{\text{JC-Stark}}^{(n,-)}$, thus the GS lies in the competition among the corresponding states in branch $\psi_n^{(-)}$ as well as ψ_0 , as shown in Fig. 1 where the orange thin lines are $E_{\text{JC-Stark}}^{(n,+)}$ (only integer- $n/5$ plotted), with $E_{\text{JC-Stark}}^0$ being the horizontal one, while the final GS is indicated by the blue line.

2. Photon Number in Low-Frequency Limit

In the low-frequency limit $\omega/\Omega \rightarrow 0$, the spacing of the quantum number n becomes small relatively to the characteristic number $n_s = x_s^2/2 = \Omega/(4\omega)$, where $x_s = \sqrt{2}g_s/\omega = \sqrt{\Omega/(2\omega)}$, which is the order of photon number induced by a coherent state in the displaced potential. In such a situation we can approximately regard the energy $E_{\text{JC-Stark}}^{(n,-)}$ as a continuous function of n . As illustrated in Fig. 1b, the minimization of $E_{\text{JC-Stark}}^{(n,-)}$ with respect to n gives an optimal quantum number

$$n_{\min} = \frac{1-\chi}{2\chi} - \frac{(\bar{g}_s^2 + 4\chi)\Omega}{8\chi^2\omega} + \frac{\bar{g}_s\Omega}{8\chi^2\omega} \sqrt{\frac{\bar{g}_s^2 + 8\chi_1}{1-\chi^2}}, \quad (13)$$

with $\chi_1 = \chi[1 - (1+\chi)\frac{\omega}{\Omega}]$.

The integer number n_j nearest to n_{\min} should be the discrete quantum number of the GS after the transition which can also obtained by level crossing $E_{\text{JC-Stark}}^{(n,-)} = E_{\text{JC-Stark}}^{(n+1,-)}$ at

$$\bar{g}_s = \sqrt{-\chi + C_1 \frac{\omega}{\Omega} + \sqrt{1 - 2(1+\chi)\frac{\omega}{\Omega} + C_2 \frac{\omega^2}{\Omega^2}}}, \quad (14)$$

$$n_j = \frac{1-2\chi}{2\chi} - \frac{(\bar{g}_s^2 + 4\chi)\Omega}{8\chi^2\omega} + \frac{\bar{g}_s\Omega}{8\chi^2\omega} \sqrt{\frac{\bar{g}_s^2 + 8\chi_1 + d}{1-\chi^2}} \quad (15)$$

where $d = 16\chi^2(1-\chi^2)\omega^2/(\bar{g}_s^2\Omega^2)$, $C_1 = (1+\chi)[3-2\chi+2(1-\chi)n]/2$, $C_2 = (1+\chi)[9-7\chi+4(1-\chi)n(n+3)]$.

In the low-frequency limit, both n_{\min} and n_j approach to

$$\frac{n_{\min}}{n_s} = \frac{n_j}{n_s} = -\frac{\bar{g}_s^2 + 4\chi}{4\chi^2} + \frac{\bar{g}_s}{4\chi^2} \sqrt{\frac{\bar{g}_s^2 + 8\chi}{1-\chi^2}}. \quad (16)$$

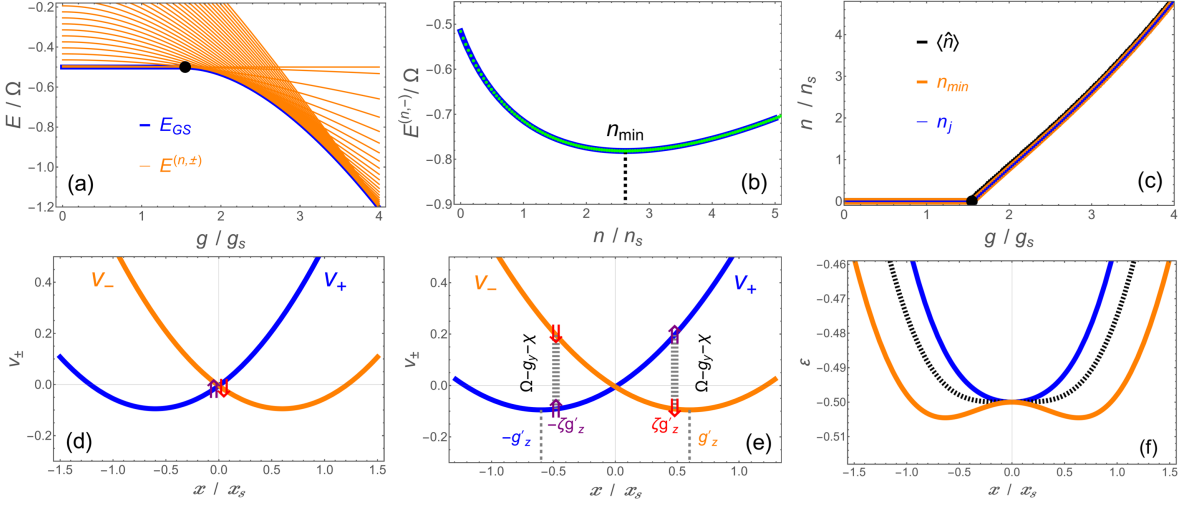


FIG. 1. *Exact solution at $\lambda = 0$ (a-c) and variational method for $\lambda \neq 0$ (d-f) in low-frequency limit with nonlinear Stark coupling.* Here $\omega = 0.01\Omega$, $\chi = 0.4$ for (a-b) and $\lambda = 0.5$ for (d-f). (a) Analytic energy spectrum versus g for excited states $E^{n,-}$ (orange thin lines) and ground state (GS) E_{GS} (blue thick line). (b) $E^{n,-}$ as a continuous (blue solid) or discrete (green dots) function of n at $g = 3g_s$, with optimized number n_{min} marked by the vertical dashed line. (c) Discrete quantum number n_j in $E^{(n_j,-)}$ (blue), optimized number n_{min} (orange) and the expectation of photon number $\langle \hat{n} \rangle$ (black) at $g = 3g_s$ for the GS. The dots in (a,c) mark the transition points $g^{\lambda,\chi}$ in the low-frequency limit. (d) Spin configuration before transition at $\chi = 0.54$, the arrows mark the positions in the effective potential for spin-up (blue, v_+) spin-down (orange, v_-) components. (e) Spin configuration after transition in v_{\pm} at $\chi = 0.74$ with variational displacements renormalized by ζ from the potential-bottom positions $\pm g'_z$ (dashed). (f) Variational energy ϵ versus the displacement x at $g = 0.8g_s$ and $\lambda = 0.5$, for $\chi = 0.54$ (blue, upper), 0.64 (dashed, middle), 0.74 (orange, lower) and the critical point is $\chi_c = 0.64$.

Figure 1c compares n_{min} (orange), n_j (blue) with the expectation of photon number $\langle \hat{n} \rangle = [nC_{n\uparrow}^{(\pm)2} + (n+1)C_{n\downarrow}^{(\pm)2}]/N$ (black) at a frequency $\omega = 0.01\Omega$, they all coincide. The result (16) will be later on used for discussion on the singular point in scaling relation.

B. Semiclassical Variational Method for $\lambda > 0$

Now let us discuss the QPTs in $\lambda > 0$ regime, while one gets the same results for $\lambda < 0$ regime in the momentum space. Note the critical coupling is of order g_s which yields a potential energy v_{σ_z} of order Ω . In the low frequency limit, the kinetic energy is of order ω , thus being relatively negligible. The Rashba spin-orbit coupling term has a strength g_y which is of order $\omega^{1/2}$ at critical couplings, also being negligible. Thus, in the leading order, we can reduce the model to a semiclassical Hamiltonian for the GS which has a zero momentum as the GS of a classical particle while the quantum part is kept in spin space:²⁶

$$H_x \rightarrow H_{SC}^x = \frac{\omega}{2} (x + g'_z \sigma_z)^2 + \epsilon_{SC}^z + \left(\frac{\Omega}{2} + \frac{\chi\omega}{2} x^2 \right) \sigma_x, \quad (17)$$

where $\epsilon_{SC}^z = -\frac{1}{2}g_z'^2\omega$. For the semiclassical approximation we have drop the zero-point energy $\frac{\omega}{2}$ in $\hat{n}\omega = \frac{\omega}{2}(\hat{x}^2 + \hat{p}^2) - \frac{\omega}{2}$ and the Stark term. From an alternative angle $\frac{\omega}{2}$ and $\frac{\chi\omega}{2}$ also can be drop due to negligible

order in the low-frequency limit. One gets similar reduced Hamiltonian H_{SC}^p of H_p for $\lambda < 0$ regime with the position x replaced by the momentum p and g'_z changed to be g'_y . We see that at infinity $x \rightarrow \infty$ the energy would be dominated by

$$H_{SC} \rightarrow \frac{\omega}{2} (1 + \chi\sigma_x) x^2 + \epsilon_{SC}^z \quad (18)$$

which is negatively unbound for $|\chi| > 1$, thus this regime is unstable and unphysical as mentioned in Section II. Hereafter we shall focus on the physical regime $|\chi| \leq 1$.

To obtain the explicit energy one can rewrite H_{SC} in a matrix form

$$H_{SC} = \begin{pmatrix} h_{\uparrow\uparrow} & h_{\uparrow\downarrow} \\ h_{\downarrow\uparrow} & h_{\downarrow\downarrow} \end{pmatrix}, \quad (19)$$

where

$$\begin{aligned} h_{\uparrow\uparrow} &= \frac{\omega}{2} (x + g'_z)^2 + \epsilon_{SC}^z, \\ h_{\uparrow\downarrow} &= \frac{\omega}{2} (x - g'_z)^2 + \epsilon_{SC}^z, \\ h_{\downarrow\downarrow} &= h_{\downarrow\uparrow} = \frac{\Omega}{2} + \frac{\chi\omega}{2} x^2. \end{aligned} \quad (20)$$

Diagonalization of H_{SC} gives two energies with the lower one being

$$\epsilon = \frac{\omega}{2} (x^2 + g_z'^2) - \frac{\omega}{2} \sqrt{4g_z'^2 x^2 + \left(x^2 \chi + \frac{\Omega}{\omega} \right)^2} + \epsilon_{SC}^z \quad (21)$$

which is still variational as the spatial position x has not yet been optimized. Minimization with respect to x

$$\frac{\partial \varepsilon}{\partial x} = 0 \quad (22)$$

leads to two solutions for the most favorable position

$$x_m^B = 0, \quad (23)$$

$$|x_m^A| = \sqrt{\frac{2g'_z}{\chi^2} \sqrt{\frac{(g_z'^2 + \chi \frac{\Omega}{\omega})}{(1 - \chi^2)}} - \frac{(2g_z'^2 + \chi \frac{\Omega}{\omega})}{\chi^2}}. \quad (24)$$

After substituting $|x_m|$ into (21) we arrive at the explicit final energies

$$E_{\text{SC}}^B = -\frac{\Omega}{2}, \quad (25)$$

$$E_{\text{SC}}^A = \varepsilon_z^z - \frac{g_z'^2 (2 - \chi^2) \omega + \chi \Omega}{2\chi^2} + \frac{g'_z (1 - \chi^2) \omega}{\chi^2} \sqrt{\frac{g_z'^2 + \chi \frac{\Omega}{\omega}}{1 - \chi^2}} \quad (26)$$

which actually are the energies before and after the phase transition, respectively, as discussed in the following.

C. Phase Diagrams and Critical Scalings in Low-Frequency limit

1. Phase Transition and Critical Boundary

Actually at a small coupling strength $|x_m^A|$ is imaginary so the only physical solution is x_m^B . Indeed, in such a situation ε has a single minimum which is located at the origin, as illustrated by the blue (upper) line in Figure 1f. The variational energy remains in the mono-minimum profile till a second-order phase transition is triggered at a critical point

$$g_c^{\lambda, \chi} = \frac{2\sqrt{(1 - \chi)}}{1 + |\lambda|} g_s = \sqrt{(1 - \chi)} g_c^\lambda, \quad (27)$$

$$|\chi_c^{\lambda, \chi}| = \frac{2\sqrt{(1 - \chi)}}{g/g_s} - 1, \quad (28)$$

$$|\chi_c^{\lambda, \chi}| = 1 - (1 + |\lambda|)^2 \frac{g^2}{4g_s^2}, \quad (29)$$

after which a double-minimum structure shows up. The black dotted line in Figure 1f shows the case right at the critical point, with a flat bottom at the origin. After the critical point, as demonstrated by the orange (lower) line, two degenerate minima appear at $\pm |x_m^A|$ while x_m^B becomes an unstable local maximum at the origin. Note the expressions for the critical point are general for both χ and λ , setting $\chi = 0$ recovers the boundary for the anisotropic QRM^{24,27}

$$g_c^\lambda = \frac{2}{1 + |\lambda|} g_s \quad (30)$$

in the absence of the Stark coupling. Setting $\lambda = 0$, the general critical boundary $g_c^{\lambda, \chi}$ reduces to the Stark-JC critical point

$$g_c^{\text{JC-Stark}} = 2g_s \sqrt{(1 - \chi)} \quad (31)$$

which is also exactly obtained by the level crossing $E_{\text{JC-Stark}}^{(0,-)} = E_{\text{JC-Stark}}^0$.

In Figure 2 we show the phase diagrams of the expectation $\langle \hat{x}^2 \rangle - \langle \hat{p}^2 \rangle$ (a,c,e) and the spin expectation $\langle \sigma_x \rangle$ (b,d,f) at a low frequency $\omega = 0.01\Omega$. The dotted curves denote the analytic critical boundary (27)-(29) which agrees well with the second-order-like transition in numerics. Figure 2a,c indicates that $\langle \hat{x}^2 \rangle - \langle \hat{p}^2 \rangle$ is anti-symmetric with respect to the sign reversal of λ , while beyond the second-order boundary (dotted) $\langle \hat{p}^2 \rangle / \langle \hat{x}^2 \rangle$ is vanishing relatively in $\lambda > 0$ regime. The ratio of $\langle \hat{x}^2 \rangle$ and $\langle \hat{p}^2 \rangle$ is reversed in $\lambda < 0$ regime, with a first-order boundary (long-dashed) at $\lambda = 0$. This scenario forms a tricritical point which is moving toward smaller-coupling direction for a positive χ and toward larger-coupling direction for a negative χ as compared with the case at $\chi = 0$ marked by the dot in Figure 2a,c.

2. Adiabatic Boundary

In the absence of the nonlinear Stark coupling, $|x_m^A|$ never goes beyond bottom of the bare potential v_{σ_z} , i.e., the displacement renormalization ratio $\zeta = x_m^A / x_{z,y}$ as indicated in Figure 1e, where $x_z = g'_z$ for $\lambda > 0$ and $x_z = g'_y$ for $\lambda < 0$, is always smaller than 1.^{23,27} Now in the presence of the Stark coupling, it may be more favorable to go farther away from the origin, and finally beyond the potential bottom at a boundary

$$|\lambda_c^{\zeta 1}| = -1 + 2\sqrt{\frac{2(1 - \chi^2)}{\chi(3 + \chi^2)} \frac{g_s}{g}}, \quad (32)$$

$$|\lambda_c^{\zeta 2}| = -1 + 2\sqrt{\frac{2}{(-\chi)} \frac{g_s}{g}}, \quad (33)$$

$$g_c^{\zeta 1} = \frac{2g_s}{1 + |\lambda|} \sqrt{\frac{2(1 - \chi^2)}{\chi(3 + \chi^2)}}, \quad (34)$$

$$g_c^{\zeta 2} = \frac{2g_s}{1 + |\lambda|} \sqrt{\frac{2}{(-\chi)}}, \quad (35)$$

for $\chi > 0$ and $\chi < 0$, respectively. We show this boundary by the dot-dashed lines in Figure 2a,c,e, as compared with the numeric boundary of $\text{sign}[1 - |\langle \hat{x}^2 \rangle - \langle \hat{p}^2 \rangle| / x_{z,y}^2]$ (note here $\langle \hat{p}^2 \rangle$ is negligible in $\lambda > 0$ regime as later on proven in Section III E). Along this boundary the effective particle keeps staying at the potential bottom position, which is adiabatic in the sense that the particle is always following the potential.

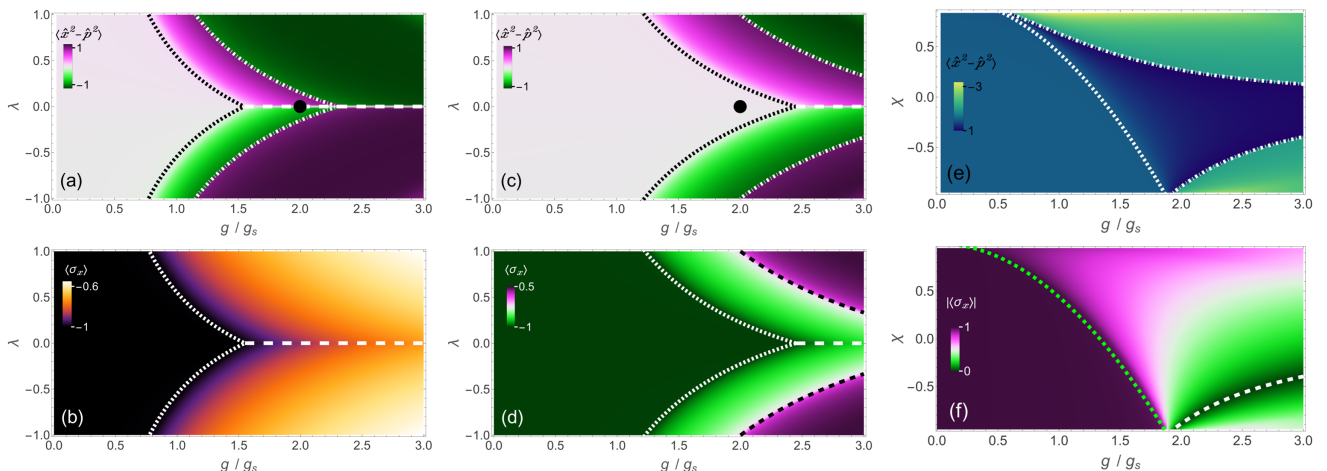


FIG. 2. GS phase diagrams in the low-frequency limit. Density plots in the g - λ plane and the g - χ plane for $\langle \hat{x}^2 \rangle - \langle \hat{p}^2 \rangle$ (a,c,e) and the spin expectation $\langle \sigma_x \rangle$ (b,d,f) with a fixed $\chi = 0.4$ (a,b), $\chi = -0.5$ (c,d), and $\lambda = 0.5$ (e,f). Here $\omega = 0.01\Omega$. To visualize the numerical boundaries better, $\langle \hat{x}^2 \rangle - \langle \hat{p}^2 \rangle$ is scaled by $x_{z,y}^2$ and timed with $\text{sign}[1 - |\langle \hat{x}^2 \rangle - \langle \hat{p}^2 \rangle|/x_{z,y}^2]$, while in (d) the amplitude is amplified by $|\langle \sigma_x \rangle|^{1/3}$. Apart from the JC line (horizontal long-dashed), the dotted, dashed, and dot-dashed curves are analytic boundaries $g_c^{\lambda,\chi}$ (27), $g_c^{\sigma_x}$ (37), and $g_c^{\zeta^i}$ (34,35), respectively.

3. Vanishing- $\langle \sigma_x \rangle$ Boundary and Coincidence with Adiabatic boundary

As mentioned in Section II, $\langle \sigma_x \rangle$ reflects flipping in the spin space and tunneling in the spatial space. Figure 2b,d show $\langle \sigma_x \rangle$ which, unlike $\langle \hat{x}^2 \rangle - \langle \hat{p}^2 \rangle$, is symmetric with respect to λ . From the phase diagrams of $\langle \sigma_x \rangle$ we find another phase boundary in $\lambda < 0$ regime, as plotted by the dashed lines in Figure 2d,f, which separates the positive and negative regimes of $\langle \sigma_x \rangle$ at

$$|\lambda g_c^{\sigma_x}| = -1 + 2\sqrt{\frac{2}{(-\chi)} \frac{g_s}{g}}, \quad (36)$$

$$g_c^{\sigma_x} = \sqrt{\frac{2}{(-\chi)} \frac{2g_s}{|\lambda| + 1}}, \quad (37)$$

$$\chi_c^{\sigma_x} = -\frac{8}{(|\lambda| + 1)^2 (g^2/g_s^2)}, \quad (38)$$

as extracted by $\langle \sigma_x \rangle = 0$ (See analytic expression of $\langle \sigma_x \rangle$ in Eq. (41)).

Comparing Figure 2e,f one may notice the vanishing- $\langle \sigma_x \rangle$ boundary coincides with the second adiabatic boundary, $g_c^{\sigma_x} = g_c^{\zeta^2}$, as also confirmed by Equations (37) and (35). In fact, under a negative χ the Stark-coupling energy is counteracting with the tunneling energy, as one can see from the Ω term and the x^2 term in Equation (17). The vanishing- $\langle \sigma_x \rangle$ boundary marked by different parameters in (36)-(38) is the point where the Stark coupling energy $E_\Omega = \frac{\Omega}{2} \langle \sigma_x \rangle$ and the tunneling energy $E_\chi = \chi \omega \langle \hat{n} \sigma_x \rangle$ are canceling. Indeed at this point, not only the expectation of spin flipping σ_x itself is vanishing, but also the effective coefficients of σ_x cancel:

$$\langle \sigma_x \rangle = 0, \quad \frac{\Omega}{2} + \frac{\chi \omega}{2} x^2 = 0, \quad (39)$$

at $x = x_m^A$ and $g = g_c^{\sigma_x}$. Consequently the Stark coupling and tunneling term does not come to effect here and only the bare potential v_{σ_z} play the role.

Besides realizing that the sign reversal of $\langle \sigma_x \rangle$ only occurs in the negative- χ regime, as indicated by the square root $\sqrt{-2/\chi}$ in (36), we also see that the two boundaries $g_c^{(\lambda,\chi)}$ and $g_c^{\sigma_x}$ does not meet unless at $\chi = -1$, as demonstrated by the Figure 2f.

D. Scaling Relations at Fixed Stark Couplings

There exist some scaling relations for the critical behavior. The scaling relation forms a universality of critical properties in the linear anisotropic QRM,^{24,27} while some more general universality can be found in the presence of the nonlinear Stark coupling. We first consider the case at fixed nonlinear Stark couplings. In the low-frequency limit, after the transition at $g_c^{(\lambda,\chi)}$ we see the effective spatial position in n -order

$$\frac{\langle \hat{x}^n \rangle}{2^{n/2} x_s^n} = \left(-\frac{\bar{g}_\lambda^2 + \chi}{\chi^2} + \frac{\bar{g}_\lambda}{\chi^2} \sqrt{\frac{\bar{g}_\lambda^2 + 2\chi}{1 - \chi^2}} \right)^{n/2}, \quad (40)$$

for the positive- λ regime and similarly $\langle \hat{p}^n \rangle$ for the negative- λ regime, while it is vanishing before the transition. Here we have defined $x_s = \sqrt{2}g_s/\omega$ and $\bar{g}_\lambda = g/g_c^\lambda = \sqrt{1 - \chi} \bar{g}_{\lambda,\chi}$, where $\bar{g}_{\lambda,\chi} = g/g_c^{\lambda,\chi}$. So, the scaled expression (40) is a function of \bar{g}_λ or $\bar{g}_{\lambda,\chi}$, thus being universal for all values of λ . Figure 3a illustrates the numerical expectation $\langle \hat{x}^2 \rangle$ for different anisotropies at a given

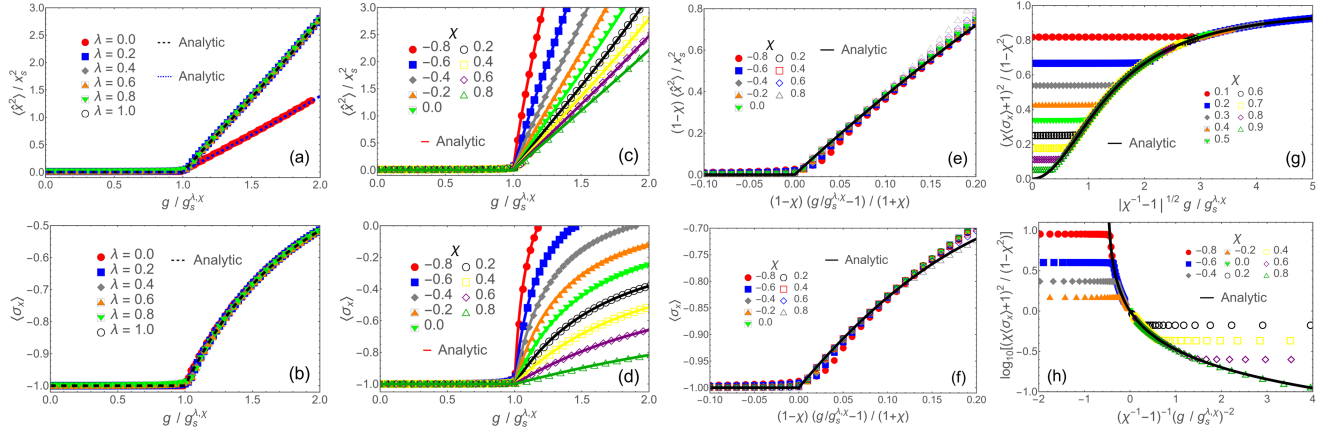


FIG. 3. *Different levels of scaling relations in the low-frequency limit.* (a,b) various λ at a fixed χ . (c-h) various χ at a fixed λ . (a) $\langle \hat{x}^2 \rangle / x_s^2$ versus $g/g_s^{\lambda, \chi}$ at $\chi = 0.4$. (b) $\langle \sigma_x \rangle$ versus $g/g_s^{\lambda, \chi}$ at $\chi = 0.4$. (c) $\langle \hat{x}^2 \rangle / x_s^2$ versus $g/g_s^{\lambda, \chi}$ at $\lambda = 0.5$. (d) $\langle \sigma_x \rangle$ versus $g/g_s^{\lambda, \chi}$ at $\lambda = 0.5$. (e) $(1-\chi)\langle \hat{x}^2 \rangle / x_s^2$ versus $(1-\chi)(g/g_s^{\lambda, \chi} - 1)/(1+\chi)$ around transition at $\lambda = 0.5$. (f) $\langle \sigma_x \rangle$ versus $(1-\chi)(g/g_s^{\lambda, \chi} - 1)/(1+\chi)$ around transition at $\lambda = 0.5$. (g) $(\chi\langle \sigma_x \rangle + 1)^2 / (1-\chi^2)$ versus $|\chi^{-1} - 1|^{1/2} g/g_s^{\lambda, \chi}$ at $\lambda = 0.5$. (h) $\log_{10}[(\chi\langle \sigma_x \rangle + 1)^2 / (1-\chi^2)]$ versus $|\chi^{-1} - 1|^{-1} (g/g_s^{\lambda, \chi})^{-2}$ at $\lambda = 0.5$. Here $\omega = 0.01\Omega$ for (a,b,c,d,g,h) and $\omega = 0.001\Omega$ for (e,f)

Stark coupling $\chi = 0.4$ for a low frequency $\omega = 0.01\Omega$, one sees that with the scaling $g/g_s^{\lambda, \chi}$ for the coupling strength and $\langle \hat{x}^2 \rangle / x_s^2$ for the quadratic position all data of different anisotropies collapse into a single line, except the JC case $\lambda = 0$. The analytic scaling relation (40) is plotted by the black dashed line which coincides with the numerics.

We also find the critical scaling relation for the spin expectation

$$\langle \sigma_x \rangle = \frac{1}{\chi} \left(-1 + \bar{g}_\lambda \sqrt{\frac{1-\chi^2}{2\chi + \bar{g}_\lambda^2}} \right) \quad (41)$$

which is also independent of λ and agrees well with the numerical scaling data, as shown in Figure 3b where all anisotropy cases collapse into a single line, including $\lambda = 0$. We see that the scaling of $\langle \sigma_x \rangle$ with respect to the anisotropy is more universal than $\langle \hat{x}^n \rangle, \langle \hat{p}^n \rangle$ in the sense there is no discontinuity at the point $\lambda = 0$ in $\langle \sigma_x \rangle$. The difference comes from the fact that $\langle \hat{x}^n \rangle$ and $\langle \hat{p}^n \rangle$ suffer from a spontaneous symmetry breaking of the duality exchange²⁷ while σ_x remains unaffected in the duality exchange.

E. Symmetry Breaking and Singularity in the $\langle \hat{x}^2 \rangle$ -Scaling Relation around $\lambda = 0$

As seen from H_x and H_p in Section II the $\lambda = 0$ case has an x - p duality symmetry which is however broken once a non-zero value of λ is introduced. It is this symmetry breaking that leads to the singular behavior of $\lambda = 0$ in the scaling relation of $\langle \hat{x}^2 \rangle$ afore-mentioned in Sec. III D. Here we shall clarify the mechanism more explicitly.

For the $\lambda = 0$ case, from the exact wavefunction (7) we see the expectations are indeed equal in accor-

dance with the x - p duality symmetry, $\langle \hat{x}^2 \rangle = \langle \hat{p}^2 \rangle = [(n + \frac{1}{2})C_{n\uparrow}^{(\pm)2} + (n + \frac{3}{2})C_{n\downarrow}^{(\pm)2}]/N$ with n substituted by n_{\min} in (13), which approach to

$$\frac{\langle \hat{x}^2 \rangle_{\lambda=0}}{x_s^2} = \frac{\langle \hat{p}^2 \rangle_{\lambda=0}}{x_s^2} = -\frac{\bar{g}_\lambda^2 + \chi}{\chi^2} + \frac{\bar{g}_\lambda}{\chi^2} \sqrt{\frac{\bar{g}_\lambda^2 + 2\chi}{1-\chi^2}} \quad (42)$$

in the low-frequency limit. Figure 3a shows the agreements of analytic result (blue dotted line) of (42) and the numerics (red dots).

Once away from the $\lambda = 0$ line, the symmetry breaking leads to an imbalance of $\langle \hat{x}^2 \rangle$ and $\langle \hat{p}^2 \rangle$, as we can see from a comparison of the energy H_{SC}^x and H_{SC}^p in (17). In fact, the minimized energy of H_{SC}^x and H_{SC}^p as in (26) can be unified to be a same function of g'_{zy}

$$E_{SC}^A(g'_{zy}) = -\frac{1}{2}g_{zy}^{\prime 2}\omega - \frac{g_{zy}^{\prime 2}(2-\chi^2)\omega + \chi\Omega}{2\chi^2} + \frac{g'_{zy}(1-\chi^2)\omega}{\chi^2} \sqrt{\frac{g_{zy}^{\prime 2} + \chi\frac{\Omega}{\omega}}{1-\chi^2}}, \quad (43)$$

with $g'_{zy} = g'_z$ for H_{SC}^x and $g'_{zy} = g'_y$ for H_{SC}^p . E_{SC}^A as a function of g'_{zy} has a maximum point $g'_{zy, \max}$ at

$$g'_{zy, \max} = g'_{zy, c} = \sqrt{(1-\chi)\Omega/(2\omega)} \quad (44)$$

which happens to be the critical point $g'_{zy, c}$ for the transition as decided by $E_{SC}^A = E_{SC}^B$. After the transition E_{SC}^A becomes a decreasing function of g'_{zy} , which can be seen from the derivative $\partial E_{SC}^A / \partial g'_{zy} = d_A - d_B$, where $d_A^2 - d_B^2 = -C_d(g_{zy}^{\prime 2} - g_{zy, \max}^{\prime 2})[g_{zy}^{\prime 2} + (1+\chi)\Omega/(2\omega)]$ and $C_d = 4\omega^2/[\chi^2(g_{zy}^{\prime 2} + \chi\frac{\Omega}{\omega})]$, being negative after $g'_{zy, \max}$. Thus, a larger value of g'_{zy} provided by g'_z and g'_y will be more favorable for the candidate of the GS.

Note in the positive- λ regime $g_z = \frac{(1+\lambda)}{2}g$ has a larger value than $g_y = \frac{(1-\lambda)}{2}g$, consequently H_{SC}^x provides a lower energy than H_{SC}^y due to the decreasing function $E_{\text{SC}}^A(g'_{zy})$. As a result, the GS from H_{SC}^x has a vanishing $\langle \hat{p}^2 \rangle$ but a finite $\langle \hat{x}^2 \rangle$ in (40) that is twice of $\langle \hat{x}^2 \rangle_{\lambda=0}$ in (42), as in the contrast displayed in Figure 3a. Reversely in the negative- λ regime, $\langle \hat{x}^2 \rangle$ is vanishing and $\langle \hat{p}^2 \rangle$ is finite as g_y is larger than g_z .

From the above discussion we see that the singular behavior in the $\langle \hat{x}^2 \rangle$ -scaling relation is a consequence of the difference from half weights of $\langle \hat{x}^2 \rangle$ and $\langle \hat{p}^2 \rangle$ for $\lambda = 0$, full weight of $\langle \hat{x}^2 \rangle$ for $\lambda > 0$, and full weight of $\langle \hat{p}^2 \rangle$ for $\lambda < 0$, in the x - p duality symmetry breaking. We can get rid of the singular behavior and get a more unified scaling relation

$$\frac{\langle \hat{x}^2 \rangle + \langle \hat{p}^2 \rangle}{x_s^2} = 2 \left(-\frac{\bar{g}_\lambda^2 + \chi}{\chi^2} + \frac{\bar{g}_\lambda}{\chi^2} \sqrt{\frac{\bar{g}_\lambda^2 + 2\chi}{1 - \chi^2}} \right), \quad (45)$$

which holds for any anisotropy including $\lambda = 0$, as shown in Figure 4a.

F. Local Scaling Relations for Various Stark Couplings around Transition

In the last two sections we have extended the scaling relation with respect to anisotropy from the absence to the presence of nonlinear Stark coupling. A more general scaling relation would be universal not only for all anisotropies but also for various Stark couplings. The λ -universal scaling relations (40) and (41) are however not unified for different values of χ , as shown in Figure 3c,d. A general scaling relation universal for both λ and χ holding globally for any strength of coupling is not readily available. Nevertheless, since critical exponent depends on the behavior in the vicinity of the transition, we can extract some scaling relations around the transition by expansion

$$\frac{(1 - \chi) \langle \hat{x}^2 \rangle}{2\hat{x}_s^2} = 2d\bar{g}_{\lambda,\chi,\omega} - d\bar{g}_{\lambda,\chi,\omega}^2 + O(d\bar{g}_{\lambda,\chi,\omega}^3) \quad (46)$$

$$\langle \sigma_x \rangle = -1 + 2d\bar{g}_{\lambda,\chi,\omega} - 3d\bar{g}_{\lambda,\chi,\omega}^2 + O(d\bar{g}_{\lambda,\chi,\omega}^3) \quad (47)$$

where $d\bar{g}_{\lambda,\chi,\omega} = \frac{1-\chi}{1+\chi} \left(\frac{g}{g_c^{\lambda,\chi}} - 1 \right)$, which are pure functions of $d\bar{g}_{\lambda,\chi,\omega}$ independent of λ, χ, ω in the first two orders. We present a comparison of the analytic scaling (46) and (47) with the numerical data in Figure 3e,f. The comparison shows that the scaling relations basically hold for different values of χ indeed, except near the unphysical limit $\chi = 1$ due to the singular third-order term which takes the form of $2d\bar{g}_{\lambda,\chi,\omega}^3(2 - 3\chi)/(1 - \chi)$.

G. Global Scaling Relation for Various Stark Couplings after Transition

Still, a more robust scaling relation can be obtained for $\langle \sigma_x \rangle$, universal for λ, χ and low frequencies without limitation of χ or the critical regime around the transition. In fact we find that the following scaling relation after the transition

$$\frac{(\chi \langle \sigma_x \rangle + 1)^2}{1 - \chi^2} = \frac{1}{2\chi\bar{g}_\lambda^{-2} + 1} = \frac{1}{2[(\chi^{-1} - 1)\bar{g}_{\lambda,\chi}^2]^{-1} + 1}. \quad (48)$$

Figure 3g shows the scaling relation (48) as a function of $\sqrt{(\chi^{-1} - 1)\bar{g}_{\lambda,\chi}}$. Here in the figure the horizontal symbols are the numeric data before the phase transition, while in the critical regime after the phase transition all data in different values of χ collapse into a same line which coincides with the analytic scaling (48). Note here the values of χ are positive, while negative χ also has a similar scaling behavior but in a different branch. Nevertheless both negative and positive χ can be finally unified in a scaling as a function of $(\chi^{-1} - 1)^{-1}\bar{g}_{\lambda,\chi}^{-2}$, as in Figure 3h. Note that the variation in λ has been scaled without any limitation as shown both numerically and analytically in Sec. IIID, thus the scaling (48) is valid for both λ and χ .

These scaling relations indicate that the properties in the critical regime obey a universal law, despite that the parameters are different in the anisotropy, the Stark coupling ratio and the frequencies (in low frequencies).

IV. BREAKING DOWN OF CRITICAL UNIVERSALITY AT FINITE FREQUENCIES

As addressed in Secs. IIID-IIIF, all levels of the scaling relations are valid under the condition of low-frequency limit. At finite frequencies the critical universality will break down and different scenarios arise. Indeed, as illustrated in Figure 4b at a finite frequency $\omega = 0.5\Omega$ for a fixed Stark coupling $\chi = 0.2$, the expectations $\langle \hat{x}^2 \rangle + \langle \hat{p}^2 \rangle$ in different ratios of anisotropy are not collapsing into a single line any longer. We see that $\langle \hat{x}^2 \rangle + \langle \hat{p}^2 \rangle$ in different λ not only increases in various gradients but also fragment into disconnected sections. At the section breakings actually emerging are a series of first-order phase transitions. Note here that fixing the Stark coupling as in Figure 3a,b is the lowest level of scaling. Now even the lowest level of scaling relation has broken down, not to mention the collapse of the higher levels of scaling relations under both various anisotropies and different nonlinear Stark couplings in Figure 3e-h. Thus we see the critical universality collapses and the systems properties are dominant by diversity which, opposite to universality with common feature, is the quality to be diverse or different.

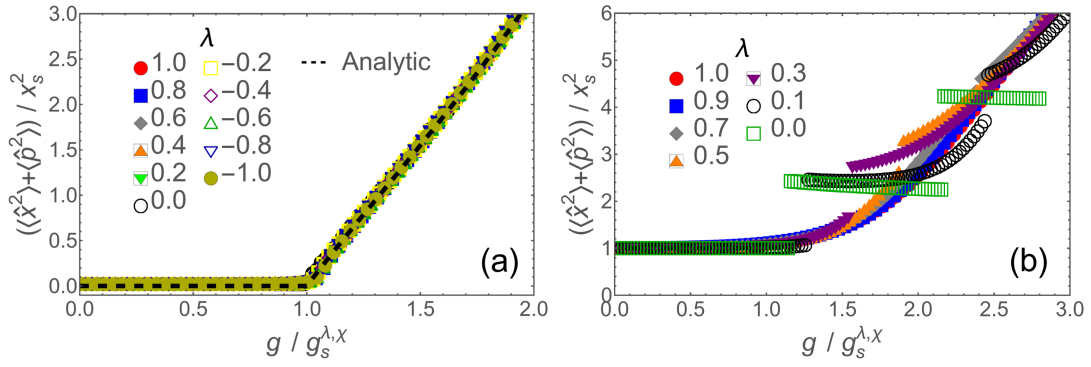


FIG. 4. *Breaking down of the critical universality at finite frequencies.* (a) Critical scaling relation for $\langle \hat{x}^2 \rangle + \langle \hat{p}^2 \rangle$ universal for all anisotropy ratios λ at a low frequency $\omega = 0.01\Omega$. (b) Breaking down of the critical universality at a finite frequency $\omega = 0.5\Omega$. Here $\chi = 0.2$ in (a,b).

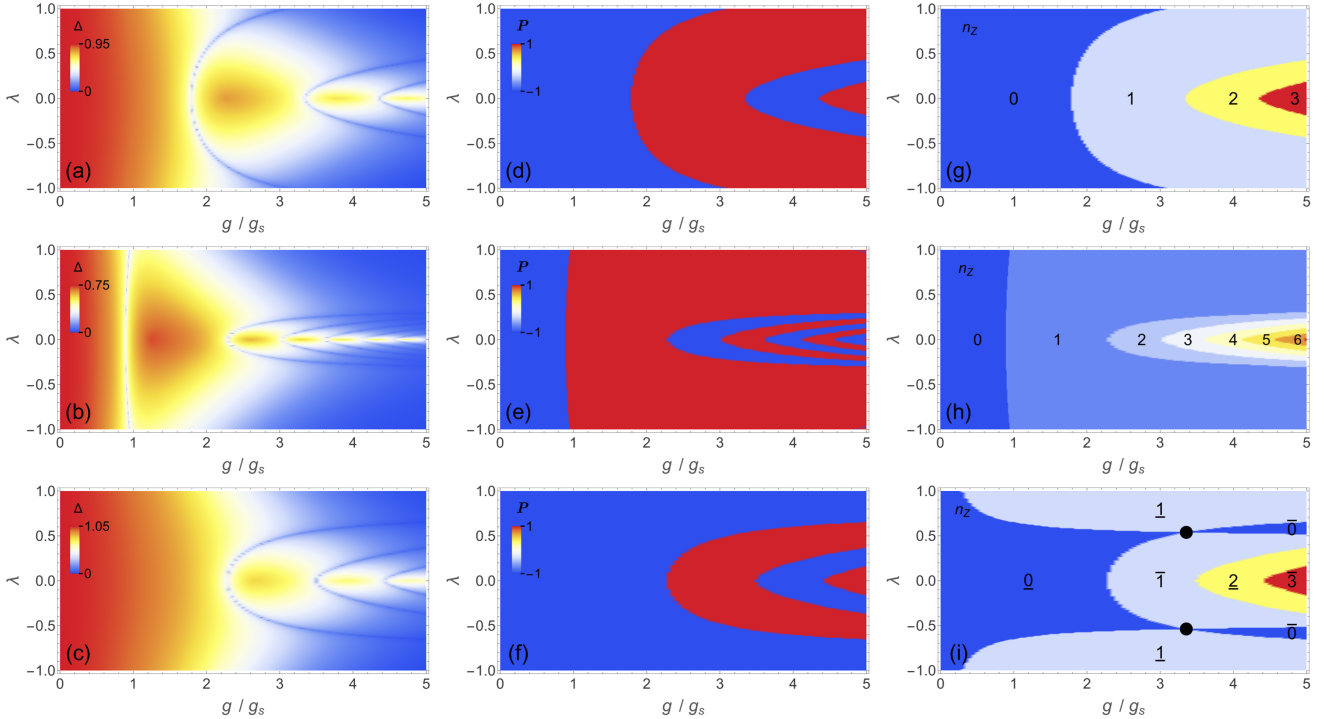


FIG. 5. *Topological classification and topological quadruple point at a finite frequency $\omega = 0.5\Omega$ with fixed Stark couplings.* The first excitation gap Δ (a-c), the GS parity P (d-f), and the GS node number n_Z (g-i) at fixed Stark couplings $\chi = 0.2$ (a,d,g), $\chi = 0.8$ (b,e,h), and $\chi = -0.3$ (c,f,i). The numbers in (g-i) are n_Z , while the overlines and underlines in (i) represent negative and positive parities. The black dots mark the topological quadruple points $\{g_{TQ}, \lambda_{TQ}\}$ (55).

V. TOPOLOGICAL CLASSIFICATION AT FINITE FREQUENCIES

Although the critical universality in low frequencies breaks down at finite frequencies and the properties are diversified, among the diversity we can still extract some common feature but from the topological structure of the GS wave function.^{27,28} Indeed, within each emerging phase at finite frequencies the GS wave function has a same node number, i.e. the number of zeros n_Z . Wave functions with different node numbers are topologically

different in the sense that, by fixing a node number n_Z , one cannot go to another n_Z state by continuous shape deformation of the wave function, just as one cannot change a torus into a sphere by a continuous deformation which is a well-known illustration for topological difference. Nodes of polynomial functions are also related to topological Galois theory in connecting algebra to topology.⁹¹ The node number is the same universally for all system parameters within a phase. This leads us to a topological classification which is not only valid for the linear anisotropic QRM^{27,28} but also in the presence

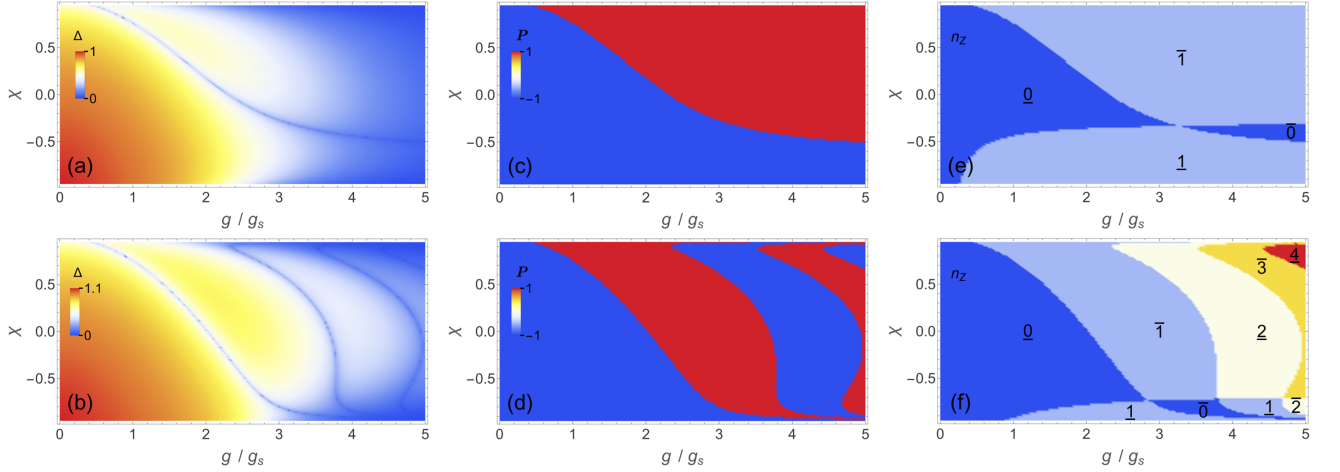


FIG. 6. *Topological classification and topological quadruple points at a finite frequency $\omega = 0.5\Omega$ with fixed anisotropy strengths. The first excitation gap Δ (a,b), the GS parity (c,d), and the GS node number (e,f) at $\lambda = 0.5$ (a,c,e), $\lambda = 0.15$ (b,d,f).*

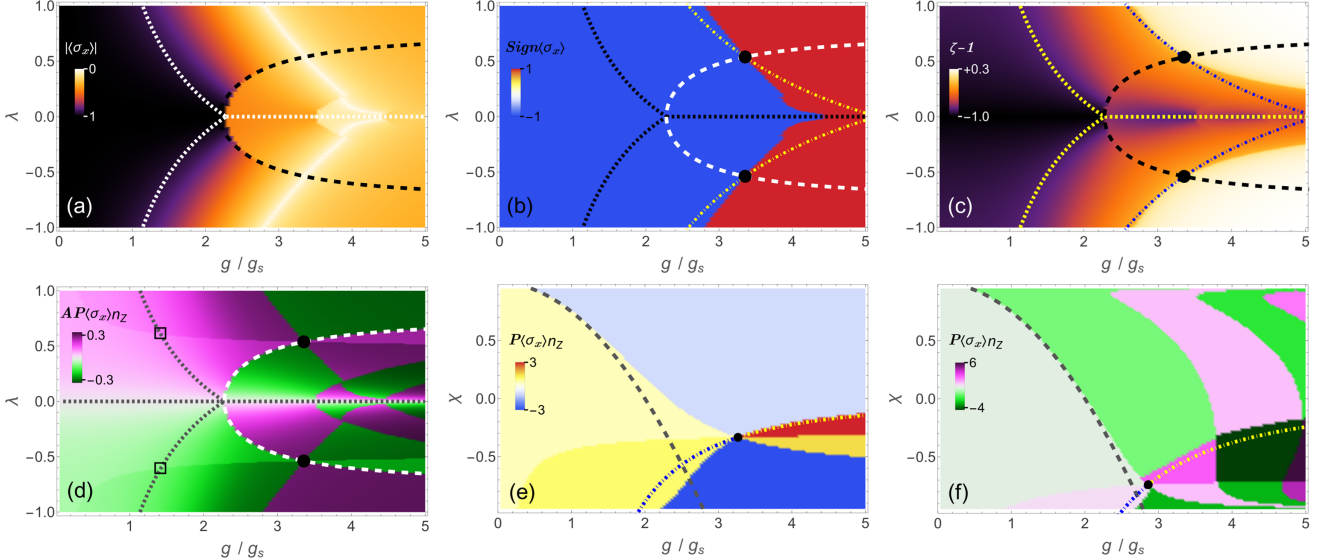


FIG. 7. *Composite phase diagrams: multicriticality, topological quadruple points, composite hexaple points, and $\langle\sigma_x\rangle$ -invariant points. a) Amplitude of $\langle\sigma_x\rangle$ in g - λ plane, plotted by $|\langle\sigma_x\rangle|^{1/2}$. b) Sign of $\langle\sigma_x\rangle$. c) $\zeta - 1$, with amplitude amplified by $|\zeta - 1|^{1/3}$. d) Composite phase diagram of $B_1 = (1 + n_z)^{1/4} \text{sign}(\langle\sigma_x\rangle)PA$. Here $\chi = -0.3$ in a-d), P is the parity and $A = \langle a^\dagger a^\dagger \rangle / A_0$ as defined in Figure 2. e) $B_2 = (1 + n_z)P[1/2 + \text{sign}(\langle\sigma_x\rangle)]$ in g - χ plane at $\lambda = 0.5$. f) B_2 at $\lambda = 0.15$. $\omega = 0.5\Omega$ in all panels. The dotted lines in (a-d) are $g_c^{\lambda,\chi}$, while horizontal ones are symmetric lines at $\lambda = 0$. The dashed lines are $g_{T1}^{\lambda,\chi}$ (49) in (a) and $g_{T1,E}^{\lambda,\chi}$ (52) in (b-d). In (b-f) the dot-dashed lines are $g_c^{\sigma_x} = g_c^{\zeta^2}$ (37,35) in low-frequency limit and the black dots mark $\{g_{TQ}, \lambda_{TQ} \text{ or } \chi_{TQ}\}$ (55,56). The dashed lines in (e-f) are $g_c^{\text{JC-Stark}}$ (31).*

of the nonlinear Stark coupling as shown in the following. On the other hand, nonlinear coupling will lead us to new phenomena unexpected in linear coupling, such as topological quadruple points, composite sextuple points and $\langle\sigma_x\rangle$ -invariant points.

A. Conventional Topological Transitions with Gap Closing

Figure 5a-c show the first excitation gap Δ in the g - λ plane for $\omega = 0.5\Omega$ at a fixed Stark coupling ratio $\chi = 0.1, 0.4, -0.3$. We see that some series of boundaries emerge where the gap is actually closing and re-opening. Figure 5d-f show the phase diagrams of parity correspondingly, with the negative and positive parities represented by the colors in blue and red, respectively.

Comparing Figure 5d-f with Figure 5a-c we see that the parity is reversed at the gap closing boundaries. Note the parity has only two values which are not enough to distinguish the series phases that emerge with the series of transitions. Something beyond the parity is needed to understand the nature of the transitions, which turns out to be topological structure of the wave function. Indeed, the node number n_Z of the GS wave function changes across each boundary of the gap closing and parity reversal, as shown by Figure 5g-i where the numbers mark n_Z of different phases. These transitions are analogs of the conventional TPTs that occurs at gap closing without symmetry breaking.²⁷

B. Unconventional Topological Transitions without Gap Closing

Besides the conventional TPTs with gap closing, unconventional TPTs may also occur without gap closing. Figure 5i shows the phase diagram of node number at a negative Stark coupling ratio $\chi = -0.3$. We see that, besides the transitions at the gap closing and parity reversal corresponding to Fig. 5c,f, there are two boundaries that have no match of either gap closing or parity change. **Figure 6** shows the phase diagrams in the g - χ plane at fixed anisotropy strengths $\lambda = 0.15$ (a,c,e) and $\lambda = 0.5$ (b,d,f). We see that besides the conventional transitions with gap closing and parity reversal, a transition boundary of node number without gap closing is also showing up in the negative- χ regime.

These additional transitions are analogs of the unconventional TPTs without gap closing in condensed matter which may occur in some particular situations, such as in the presence of a strong electron-electron interaction in the quantum spin Hall effect⁹² or in the presence of disorder with Berry curvature separation in the quantum anomalous Hall effect.⁹³

C. Topological Quadruple Points

In the absence of the nonlinear Stark coupling the unconventional TPTs occur in $\lambda > 1$ regime.²⁸ Here we see that the nonlinear Stark coupling is bringing the unconventional TPTs from the regime beyond the QRM line ($\lambda = 1$) to the intermediate regime $0 < \lambda \leq 1$ between the QRM and the JCM which are the most fundamental models in light-matter interactions. The entering of the unconventional TPTs into the intermediate regime has two consequences: On the one hand, the TPTs can occur in the isotropic QRM with weak couplings, as indicated by Figure 5i; On the other hand, some topological quadruple points are formed, as one finds in Figure 5i and Figure 6e,f.

Note that the node number characterizes the topological structure of the wave function within a same spin component, while the parity reflects the relative struc-

ture between the two spin components. In the phase labels of Figure 5i and Figure 6e,f we have combined the node number and the parity to distinguish the phases better from each other. We see that four topological phases meet at a topological quadruple point, e.g. in Figure 5i, marked by dots around which two phases have $n_Z = 0$ and the other two have $n_Z = 1$ while the parity is different for the phases with a same node number. Such topological quadruple points mean the boundary crossing of the conventional TPTs with gap closing and unconventional TPTs without gap closing, which never happens for the linear interaction in the absence of the nonlinear Stark coupling.²⁸

D. Composite Phase Diagrams: Multicriticality, Composite Quadruple Points, Composite Sextuple Points

We have seen in Figure 5 that P and n_Z , are symmetric with respect to the sign reversal of λ as it is also true for $\langle \sigma_x \rangle, \zeta$ discussed in Section III C, while $\langle \hat{x}^2 \rangle - \langle \hat{p}^2 \rangle$ is antisymmetric in Figure 2a,c. Here at a finite frequency ζ is extracted by ratio of the main-peak position of $\psi_{\pm}(x)$ and the potential-bottom position g'_z for $\lambda > 0$ (g'_y for $\lambda < 0$). Combining these quantities for an overview will expose some underlying features.

Hexacritical point: In **Figure 7d** we present a density plot for the composite quantity $(n_Z + 1)^{1/4} P(\langle \hat{x}^2 \rangle - \langle \hat{p}^2 \rangle) \text{sign}(\langle \sigma_x \rangle)$ in the g - λ plane at $\omega = 0.5\Omega$ and $\chi = -0.3$. Along the symmetric $\lambda = 0$ line, one sees first a hexacritical point around $g = 2.3g_s$ which is the crossing point of the first-order boundary (white dashed line, see expressions in (49,52)) and the second-order boundary $g_c^{\lambda,x}$ (black dotted curves, (27)) as more reflected by the amplitude of $\langle \sigma_x \rangle$ in Figure 7a.

Composite quadruple/sextuple points: Along the $\lambda = 0$ line following the afore-mentioned hexacritical point are a composite quadruple point around $g = 3.5g_s$ and a composite sextuple point around $g = 4.5g_s$, while increasing g one would see more composite quadruple points beyond the plotting range. The composite sextuple point is actually a quadruple point (not topological quadruple point) in $n_Z P(\langle \hat{x}^2 \rangle - \langle \hat{p}^2 \rangle)$ but the sign-reversal boundary of $\langle \sigma_x \rangle$ renders it to be a sextuple-like point. The $\langle \sigma_x \rangle$ -sign-reversal boundary as shown in Figure 7b also leads to another composite quadruple point away from the $\lambda = 0$ line around $\{g/g_s, \lambda\} = \{3.8, 0.2\}$ in Figure 7c.

Meeting of second-order transition and unconventional TPT: The composite multiple points addressed above are located at the conventional TPT boundaries which are in principle of first order with gap closing. Another two composite quadruple points we did not stress are the crossing points of the boundary $g_c^{\lambda,x}$ (dotted curves) and the unconventional TPT boundary, around $\{g/g_s, \lambda\} = \{1.4, \pm 0.6\}$ as marked by the empty squares in Figure 7d. The critical transition at $g_c^{\lambda,x}$ is second-order, which is softened at finite frequencies but still has

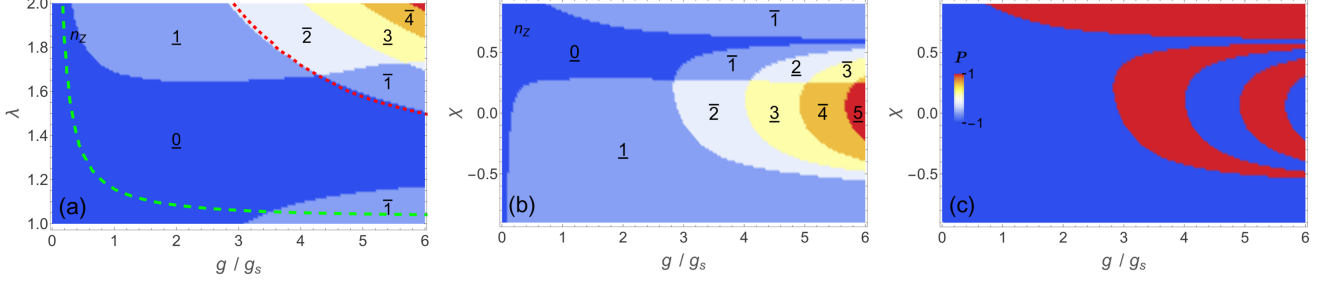


FIG. 8. Phase diagrams in large- λ regime at $\omega = 0.5\Omega$. a) n_Z in g - λ plane at $\chi = 0.1$. b) n_Z in g - χ plane at $\lambda = 2.0$. c) P at $\lambda = 2.0$. The numbers mark n_Z with underlines and overlines representing negative and positive parities. The dashed line and dotted line in (a) are respectively the $\underline{0}/\underline{1}$ and $\underline{1}/\underline{2}$ boundaries at $\chi = 0$.

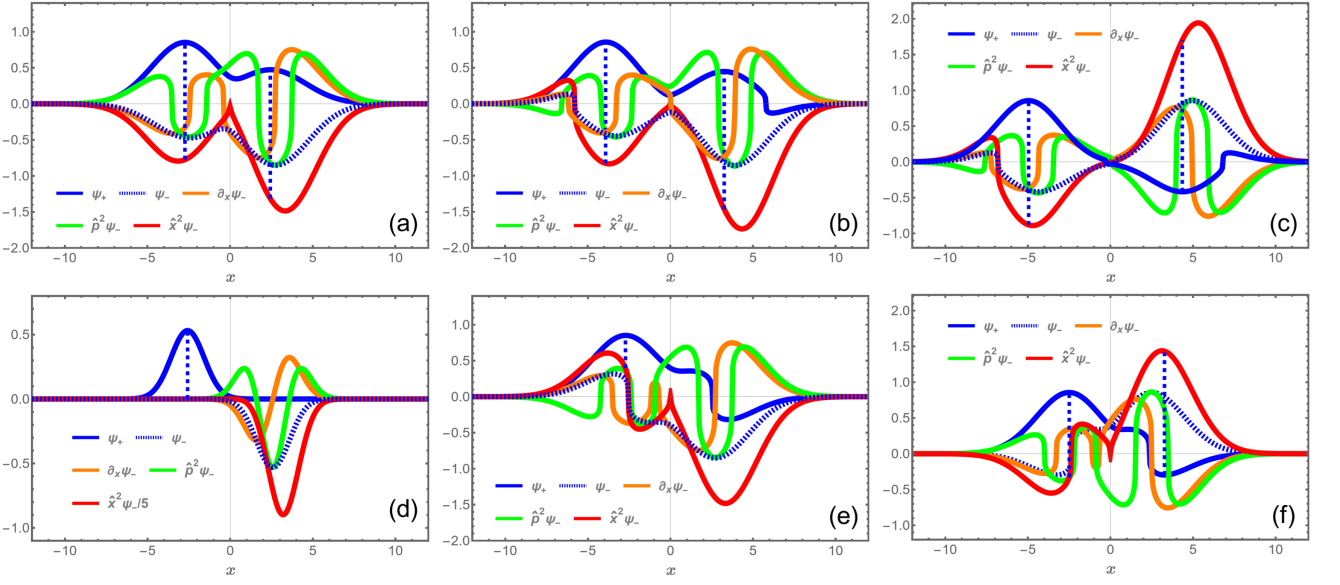


FIG. 9. Mechanism analysis: GS wave function and energy competitions. ψ_+ (blue solid), ψ_- (blue dotted), $\partial_x \psi_-$ (orange), $\hat{p}^2 \psi_-$ (green), $\hat{x}^2 \psi_-$ (red) in x space at a) $\chi = 0.1$, $\lambda = 1.1$, $g = 2.6g_s$ ($P = -1$, $n_Z = 0$), b) $\chi = 0.1$, $\lambda = 2.0$, $g = 2.6g_s$ ($P = -1$ and $n_Z = 1$), c) $\chi = 0.1$, $\lambda = 2.0$, $g = 3.3g_s$ ($P = 1$ and $n_Z = 2$), d) $\chi = -0.3$, $\lambda = 0.538$, $g = 3.355g_s$ ($P = -1$ and $n_Z = 0$), e) $\chi = -0.3$, $\lambda = 0.8$, $g = 3.0g_s$ ($P = -1$ and $n_Z = 1$), f) $\chi = -0.3$, $\lambda = 0.4$, $g = 3.6g_s$ ($P = 1$ and $n_Z = 1$). The vertical dashed lines mark the peak positions of ψ_+ . In all panels $\omega = 0.5\Omega$ and except (d) the amplitude A_m in each line is amplified by $A_m^{1/4}$ for better visibility.

a remnant of superradiant transition in photon number.²⁸ The unconventional TPT would be infinite-order.

E. Composite Phase Diagrams: Topological Quadruple Point being $\langle \sigma_x \rangle$ -Invariant Point

Apart from the afore-mentioned composite sextuple point formed from the non-topological quadruple point and the $\langle \sigma_x \rangle$ -sign-reversal boundary, more special is another composite sextuple point around $\{g/g_s, \lambda\} = \{3.36, 0.538\}$ (with its dual point at $\{3.36, -0.538\}$ in $\lambda < 0$ regime), as marked by the dots in Figure 7d. This second composite sextuple point previously was the first topological quadruple point of Figure 5i addressed in Section VC and now we see it happens that the conventional

TPT boundary, the unconventional TPT boundary and the $\langle \sigma_x \rangle$ -sign-reversal boundary are all crossing at the topological quadruple point to form a sextuple-like point.

The $\langle \sigma_x \rangle$ -sign-reversal boundary is also vanishing- $\langle \sigma_x \rangle$ boundary indicated by the bright line Figure 7a. Note here the frequency is finite, while the vanishing- $\langle \sigma_x \rangle$ boundary in the low-frequency limit, $g_c^{\sigma_x}$ in (36), is plotted as the dot-dashed line Figure 7b. Particularly, the topological quadruple remains invariant when the other vanishing- $\langle \sigma_x \rangle$ points are moving away from dot-dashed line in the variation of frequency. Thus we find this topological quadruple point is a $\langle \sigma_x \rangle$ -invariant point. Moreover, it is also an adiabatic-invariant as similarly displayed in Figure 7c where the dot-dashed line is adiabatic boundary $g_c^{\zeta^2}$ in the low-frequency limit, (35), while the color change around the dot-dashed line indicates the

$\zeta = 1$ boundary at the finite frequency.

In Figure 7e one can also see the sextuple-like point in a composite phase diagram of $(n_Z + 1)P[\text{sign}(\langle \sigma_x \rangle) + \frac{1}{2}]$ in the g - χ plane at a fixed $\omega = 0.5\Omega$ and $\lambda = 0.5$. As shown by Figure 7f, the sextuple degeneracy will be raised if it is located close to the Stark-JC critical boundary $g_c^{\text{JC-Stark}}$ (Equation (31) as plotted by dashed lines in Figure 7e,f). Here, unlike the leading two-peak structure both before and after transition for points away from $g_c^{\text{JC-Stark}}$, the GS wave function is however of one-peak structure before the transition and two-peak structure after,²⁷ which leads to different vanishing- $\langle \sigma_x \rangle$ points thus the dislocation of the $\langle \sigma_x \rangle$ boundaries. In contrast, the topological quadruple point is more robust and still survives there despite of the breakdown of the sextuple degeneracy

F. Analytic expressions of the first topological boundary and topological quadruple point

By adding the Stark term to the treatment on the $0/\bar{1}$ transition in the polaron picture,²⁷ we can get an analytic boundary for the first conventional TPT in the leading order

$$g_{\text{T1}}^{\lambda,\chi} = \frac{2\sqrt{2}}{\sqrt{(1+\lambda)[(2+\chi) - \lambda(2-\chi)]}} g_s, \quad (49)$$

$$\lambda_{\text{T1}} = \frac{2\sqrt{1-2(2-\chi)g_s^2/g^2 + \chi}}{2-\chi}, \quad (50)$$

$$\chi_{\text{T1}} = \frac{2[4 - (1-\lambda^2)g^2/g_s^2]}{(1+|\lambda|)^2 g^2/g_s^2}, \quad (51)$$

which provides an analytic confirmation with a direct insight about the node variation at the TPT.²⁷ From exact solution^{3,94} we can also get an accurate analytic boundary

$$g_{\text{T1,E}}^{\lambda,\chi} = \frac{2\sqrt{1-\chi^2}}{\sqrt{(1+\chi) - \lambda^2(1-\chi)}} g_s, \quad (52)$$

$$\lambda_{\text{T1,E}} = \sqrt{(1+\chi)\left[\frac{1}{1-\chi} - \frac{4}{g^2/g_s^2}\right]}, \quad (53)$$

$$\chi_{\text{T1,E}} = -\frac{1+\lambda^2}{8} \frac{g^2}{g_s^2} + \sqrt{\left[1 + \frac{1+\lambda^2}{8} \frac{g^2}{g_s^2}\right]^2 - \frac{g^2}{2g_s^2}}. \quad (54)$$

Besides recovering $g_{\text{T1}}^{\lambda,0} = \frac{2}{\sqrt{1-\lambda^2}} g_s$ at $\chi = 0$,²⁷ both $g_{\text{T1}}^{\lambda,\chi}$ and $g_{\text{T1,E}}^{\lambda,\chi}$ agree with the numeric results at a finite χ , as indicated by the dashed lines in Figure 7a-d, except for some discrepancy around $\lambda = 0$ for $g_{\text{T1}}^{\lambda,\chi}$ at a large χ .

Combining (52-54) and (36-38), we find the analytic locations of the topological quadruple points

$$g_{\text{TQ}}^{\chi} = \frac{\sqrt{2}(1-\chi)}{\sqrt{-\chi}}, \quad \lambda_{\text{TQ}}^{\chi} = \pm \frac{1+\chi}{1-\chi}; \quad (55)$$

$$g_{\text{TQ}}^{\lambda} = \frac{2\sqrt{2}}{\sqrt{1-\lambda^2}}, \quad \chi_{\text{TQ}}^{\lambda} = -\frac{1-|\lambda|}{1+|\lambda|}. \quad (56)$$

under a given Stark coupling and under a fixed anisotropy ratio respectively, which are plotted as dots and coincide with numerics in Figures 5,7.

G. Topological Quadruple Points in Large λ

So far we have focused on $|\lambda| \leq 1$ regime, while topological quadruple points can also emerge in large- λ regime. **Figure 8a,b** display the phase diagrams of n_Z , together with P represented by overlines and underlines, respectively under a given Stark coupling ratio $\chi = 0.2$ (a) and at a fixed anisotropy strength $\lambda = 2.0$ (b). For a confirmation and a more direct view, the parity is also explicitly plotted in Figure 8c at $\lambda = 2.0$. The conventional TPTs occur between phases n_Z and $n_Z \pm 1$, while the unconventional ones lie on the boundaries between phases \bar{n}_Z and $\bar{n}_Z \pm 1$ or between \underline{n}_Z and $\underline{n}_Z \pm 1$. As one sees from Figure 8a the conventional TPT boundaries remain almost unmoving in adding the Stark coupling as compared with the $\chi = 0$ boundary (dotted line). This scenario is confirmed by Figure 8b where the conventional TPTs are not much affected in the vicinity of $\chi = 0$, unless a large amplitude of χ is involved. In a strong contrast, the unconventional TPTs ($0/\bar{1}$ boundary) are very sensitive to the variation of χ , as one compares with the dashed line which represents the unconventional TPT boundary at $\chi = 0$. In the absence of the Stark coupling, the conventional and unconventional TPTs do not cross each other.²⁸ Now in adding the Stark coupling, the slow motion of the conventional TPTs and the fast moving of the unconventional TPTs result in the boundary crossing and thus bring about the topological quadruple points.

VI. MECHANISMS

To get an understanding for some key features of the different TPTs and the topological quadruple points, in **Figure 9** we show the profiles of $\psi_+(x)$, $\psi_-(x)$ and $\partial_x \psi_-$, $\hat{p}^2 \psi_-$, $\hat{x}^2 \psi_-$ in x space for GSs. They contribute to the tunneling and different interacting parts in the GS energy

$$E_{\Omega} = \frac{\Omega}{2} \int \psi_+(x) \psi_-(x) dx, \quad (57)$$

$$E_{g_y} = \sqrt{2}(-g_y) \int \psi_+(x) \partial_x \psi_-(x) dx, \quad (58)$$

$$E_{p^2} = \frac{\chi\omega}{2} \int \psi_+(x) \hat{p}^2 \psi_-(x) dx, \quad (59)$$

$$E_{x^2} = \frac{\chi\omega}{2} \int \psi_+(x) \hat{x}^2 \psi_-(x) dx, \quad (60)$$

which involve subtle competitions.

A. TPTs and quadruple points in $\lambda > 1$ regime

Node from infinity: Figure 9a-c illustrate some typical points of different phases $\underline{0}$, $\underline{1}$, $\bar{2}$ in Figure 8 in $\lambda > 1$ regime with $\chi = 0.1$. Around the isotropic line as in Figure 9a with $\lambda = 1.1$ and $g = 2.6g_s$, the amplitude of $g_y = (1 - \lambda)g/2$ is small so that E_Ω plays a more dominant role which favors a nodeless state with $n_Z = 0$ which has opposite signs of $\psi_+(x)$ and $\psi_-(x)$ in all positions. In a larger λ as in Figure 9b with $\lambda = 2.0$ and $g = 2.6g_s$, note $(-g_y)$ is positive here which also favors opposite signs of $\partial_x\psi_-$ and $\psi_+(x)$. The larger contribution of E_{gy} leads to the negative-peak replacement of ψ_- by $\partial_x\psi_-$ in alignment (as indicated by vertical dashed line) with the positive peak of $\psi_+(x)$ on the left side to get a lower energy. A node introduction from infinity will not only enhance the negative peak of $\partial_x\psi_-$ on the left but also make the tails of $\partial_x\psi_-$ and $\psi_+(x)$ opposite in sign on the right. This energy competition creates a node of $\psi_\pm(x)$ around $x = \mp 5.2$, with $n_Z = 1$. This node transition between cases (a) and (b) occurs without gap closing, being an unconventional TPT.²⁸

Unconventional TPT in $\lambda > 1$ regime sensitive to χ : In the nonlinear Stark parts, $\hat{p}^2\psi_-$ is oscillating to cancel itself to a large extent, thus the main contribution lies in $\hat{x}^2\psi_-$ (which is also a reason why it is x -type in $\lambda > 0$ regime). Note, with a node from infinity, the tails of $\hat{x}^2\psi_-$ has a same sign as $\psi_+(x)$ as in Figure 9b, which is unfavorable for E_{x^2} with a positive χ . In this sense, $\hat{x}^2\psi_-$ is counteracting with $\partial_x\psi_-$ in such a node introduction. Consequently, one needs a larger λ to strengthen the $(-g_y)$ term E_{gy} to trigger the unconventional TPT. This accounts for the far boundary moving of the unconventional TPT from around $\lambda = 0$ (dashed line in Figure 8a) in the absence of the Stark coupling to a larger λ ($\underline{0}/\underline{1}$ boundary around $\lambda = 1.7$ in Figure 8a) in the presence of a positive Stark coupling χ .

Conventional TPT in $\lambda > 1$ regime unaffected by χ : On the other hand, for the conventional TPT, Figure 9c shows the state at $\lambda = 2.0$ and a larger linear coupling $g = 3.3g_s$ after the $\underline{1}/\bar{2}$ transition from state in Figure 9b. Such a conventional TPT introduces a node around the origin $x = 0$, thus accompanied with gap closing and parity reversal. In such a situation the leading variation lies around the origin while the farther parts remain little affected. Note that $\hat{x}^2\psi_-$ and $\hat{p}^2\psi_-$ have similar decreasing amplitudes but opposite signs around the origin both before and after the transition, which leads to a cancellation effect. As a result, $\hat{x}^2\psi_-$ and $\hat{p}^2\psi_-$ together do not play much role in this conventional TPT, unless one increases χ much to multiply their difference. This explains the little moving of the conventional TPT boundaries in the variations of Stark coupling as in Figure 8 (dotted line and $\underline{1}/\bar{2}$ boundary).

Topological quadruple points: Since the conventional TPTs keeps almost unmoved while the unconventional TPT is sensitive to the introduction of the Stark coupling, their boundary meeting naturally occurs. The final

boundary crossing gives rise to the topological quadruple points.

B. TPTs and quadruple points in $\lambda < 1$ regime

Unconventional TPT in $\lambda < 1$ regime with negative χ : Now we look at the $\lambda < 1$ regime with a negative χ , as in Figure 5i. The nodeless state ($n_Z = 0$) in a small g is similar to Figure 9a with peak alignment of $\psi_+(x)$ and $\psi_-(x)$ due to the dominant E_Ω . Figure 9e shows a nodal $\underline{1}$ state in Figure 5i after the $\underline{0}/\underline{1}$ unconventional TPT. Here $(-g_y)$ is negative, different signs of $\partial_x\psi_-(x)$ and $\psi_+(x)$ are unfavorable for lowering the energy of E_{gy} . A node introduced from infinity as in Figure 9e would not only bring wave-packet tails with same signs of $\psi_-(x)$ and $\psi_+(x)$ to increase E_Ω but also lead to larger tails of $\partial_x\psi_-(x)$ and $\psi_+(x)$ with different signs on the right than the tails with same signs on the left to raise E_{gy} , so there is no unconventional TPT in the absence of Stark coupling. However, in the presence of a negative χ , on both sides $\hat{x}^2\psi_-$ has tails with same signs as ψ_+ , as in Figure 9e, which reduces the energy from E_{x^2} and makes the unconventional TPT possible. Therefore, the unconventional TPT boundary moves from $\lambda > 1$ regime to $\lambda < 1$ regime as in Figure 5i.

Conventional TPT in $\lambda < 1$ regime depending on χ : In contrast to the χ -insensitivity in $\lambda > 1$ regime the conventional TPT in $\lambda < 1$ regime depends much on χ as shown in Figures 5,6. Figure 9f shows a state in the $\bar{1}$ phase of Figure 5i. Comparing with Figure 9c one sees there is no afore-mentioned cancellation effect of $\hat{x}^2\psi_-$ and $\hat{p}^2\psi_-$ around the origin. This is because the distance of left and right wavepackets depends on $g_z = (1 + \lambda)g/2$ which is much smaller in $\lambda < 1$ regime so that there is more overlap between left and right wavepackets. Since the conventional TPT comes from the node number variation around the origin, the transition boundary is then much influenced by the Stark coupling with the enlarged difference of $\hat{x}^2\psi_-$ and $\hat{p}^2\psi_-$.

Invariant point: Actually Figure 9e,f take the points along the boundary where $\langle\sigma_x\rangle$ vanishes and changes the sign in Figure 7a,b. In these cases the wavefunction is finite in amplitude on both sides, while the vanishing of $\langle\sigma_x\rangle$ comes from the cancellation between same-sign and opposite-sign parts of $\psi_+(x)$ and $\psi_-(x)$ with a certain position of the node. Such a cancellation depends on the frequency ω since the size of wavepackets will vary with the frequency²⁶ to affect the cancellation situation. In contrast, the status of the topological quadruple point is distinctive, as one side of wavepacket is completely flat as demonstrated by Figure 9d. The vanishing of $\langle\sigma_x\rangle$ at the topological quadruple point results from the vanishing local product of $\psi_+(x)$ and $\psi_-(x)$ rather than the cancellation. In such a situation, other terms $\partial_x\psi_-$, $\hat{p}^2\psi_-$, $\hat{x}^2\psi$ do not come to effect either. Thus, the GS effectively behaves like a non-interacting particle in displaced harmonic potential ($v_{\sigma_z}(x)$ in (3)), with the particle location

adiabatically being the potential bottom position, which is the reason why here also $\zeta = 1$. Note such a status effectively being the GS of a displaced harmonic potential remains the same for different frequencies, this topological quadruple point appears as an invariant point in the sense the vanishing value of $\langle \sigma_x \rangle$ and adiabatic value $\zeta = 1$ remain unchanged when the frequency is varying.

VII. CONCLUSIONS AND DISCUSSIONS

We have investigated the critical universality and topological universality in light-matter interactions via a thorough study on the first excitation gap and the GS of the QRM generally in the presence of interaction anisotropy and nonlinear Stark coupling.

In the low-frequency limit, we have obtained both numerically and analytically all phase boundaries of the QPTs in the GS as well as the adiabatic boundaries and the vanishing- $\langle \sigma_x \rangle$ boundaries. We have extracted various scaling relations in which physical properties collapse into the same line, respectively for different anisotropy ratios under finite Stark coupling and variations of both anisotropy and Stark coupling, locally around the QPTs or globally for all coupling regions after the transitions. These scaling relations form different levels of critical universalities. It may be worthy to mention that usually critical universality concerns a same critical exponent around the transition while same coefficients are not required.⁵³ Here, the scaling relations with same-line collapsing and more global range provide a stricter universality in some sense.

At finite frequencies, the critical universality breaks down and the diversity comes to dominate. Amidst the diversity we have extracted the topological classifications which form a new universality essentially different from the critical universality. The critical universality involves the second-order transitions, while the topological universality here classifies the phases in the emerging first-order transitions for the conventional TPTs with gap closing or the infinite-order transitions for the unconventional TPTs without gap closing. Moreover, the universality-diversity-universality process demonstrates that although universality and diversity are antagonists by nature, counter-intuitively they can acquire coexist-

tence and mutual support. We stress that both the critical universality and the topological classification hold not only for the linear interaction but also in the presence of nonlinear Stark coupling, thus yielding a more robust scenario of universalities.

While the conventional TPTs and the unconventional TPTs never meet in linear QRM,²⁸ the presence of the nonlinear coupling enables boundary crossings of the conventional and unconventional TPTs, which brings about the appearance of topological quadruple points. The composite phase diagrams in combination with the vanishing- $\langle \sigma_x \rangle$ and adiabatic boundaries further display the multicriticality, composite quadruple points and composite hexaple points. In particular, we reveal that the topological quadruple points in the intermediate anisotropy regime are in fact $\langle \sigma_x \rangle$ -invariant points and adiabatically-invariant points in varying the frequency. This indicates that the locations of such topological quadruple points can be detected by invariant spin-flipping or tunneling points when one tunes the frequency.

Our phase diagrams and sensitivity analysis with respect to the nonlinear Stark coupling demonstrate that in addition to the anisotropy the nonlinear coupling provides another approach to manipulate both the critical QPTs and the TPTs. Especially, the unconventional TPTs are quite sensitive in response to the nonlinear coupling.

Experimentally in superconducting circuit systems^{77,95,96} with deep-strong couplings^{1,6-15,97,98} the effective position x and momentum p are realistically the flux and charge of Josephson junctions and the spin can be also implemented by flux qubit, the nodal status might be detected by interference devices and magnetometer.⁹⁶ In practice, the interaction anisotropy is highly tunable^{6,31,72} and the nonlinear Stark coupling can also be realized with adjustable amplitude and sign,^{30,73-75} which could provide feasible platforms for possible tests or potential applications of our results.

ACKNOWLEDGEMENTS

This work was supported by the National Natural Science Foundation of China (Grant No. 11974151).

-
- [1] P. Forn-Díaz, L. Lamata, E. Rico, J. Kono, E. Solano, *Rev. Mod. Phys.* **2019**, *91*, 025005.
 - [2] A. F. Kockum, A. Miranowicz, S. De Liberato, S. Savasta, F. Nori, *Nature Reviews Physics* **2019**, *1*, 19.
 - [3] D. Braak, *Phys. Rev. Lett.* **2011**, *107*, 100401.
 - [4] See a review of theoretical methods for light-matter interactions in A. Le Boité, *Adv. Quantum Technol.* **2020**, *3*, 1900140.
 - [5] See a review of quantum phase transitions in light-matter interactions e.g. in J. Liu, M. Liu, Z.-J. Ying, H.-G. Luo,

- Adv. Quantum Technol.* **2021**, *4*, 2000139.
- [6] P. Forn-Díaz, J. Lisenfeld, D. Marcos, J. J. Garcia-Ripoll, E. Solano, C. J. P. M. Harmans, J. E. Mooij, *Phys. Rev. Lett.* **2010**, *105*, 237001.
- [7] A. Wallraff, D. I. Schuster, A. Blais, L. Frunzio, R.-S. Huang, J. Majer, S. Kumar, S. M. Girvin, R. J. Schoelkopf, *Nature* **2004**, *431*, 162.
- [8] T. Niemczyk, F. Deppe, H. Huebl, E. P. Menzel, F. Hocke, M. J. Schwarz, J. J. Garcia-Ripoll, D. Zueco, T. Hümmer, E. Solano, A. Marx, R. Gross, *Nature Phys.*

- 2010**, *6*, 772.
- [9] G. Günter, A. A. Anappara, J. Hees, A. Sell, G. Biasiol, L. Sorba, S. De Liberato, C. Ciuti, A. Tredicucci, A. Leitenstorfer, R. Huber, *Nature* **2009**, *458*, 178.
- [10] P. Forn-Díaz, J. J. García-Ripoll, B. Peropadre, J. L. Orgiazzi, M. A. Yurtalan, R. Belyansky, C.M. Wilson, A. Lupascu, *Nat. Phys.* **2017**, *13*, 39.
- [11] B. Peropadre, P. Forn-Díaz, E. Solano, and J. J. García-Ripoll, *Phys. Rev. Lett.* **2010**, *105*, 023601.
- [12] G. Scalari, C. Maissen, D. Turčinková, D. Hagenmüller, S. De Liberato, C. Ciuti, C. Reichl, D. Schuh, W. Wegscheider, M. Beck, J. Faist, *Science* **2012**, *335*, 1323.
- [13] Z.-L. Xiang, S. Ashhab, J. Q. You, F. Nori, *Rev. Mod. Phys.* **2013**, *85*, 623. J.Q. You, F. Nori, *Phys. Rev. B* **2003**, *68*, 064509.
- [14] X. Gu, A. F. Kockum, A. Miranowicz, Y. X. Liu, F. Nori, *Phys. Rep.* **2017**, *718*, 1.
- [15] F. Yoshihara, T. Fuse, S. Ashhab, K. Kakuyanagi, S. Saito, K. Semba, *Nat. Phys.* **2017**, *13*, 44.
- [16] A. Bayer, M. Pozimski, S. Schambeck, D. Schuh, R. Huber, D. Bougeard, C. Lange, *Nano Lett.* **2017**, *17*, 6340.
- [17] I. I. Rabi, *Phys. Rev.* **1937**, *51*, 652.
- [18] E. Solano, *Physics* **2011**, *4*, 68.
- [19] F. A. Wolf, M. Kollar, D. Braak, *Phys. Rev. A* **2012**, *85*, 053817.
- [20] S. Felicetti, A. Le Boité, *Phys. Rev. Lett.* **2020**, *124*, 040404.
- [21] S. Felicetti, M.-J. Hwang, A. Le Boité, *Phys. Rev. A* **2018**, *98*, 053859.
- [22] S. Ashhab, *Phys. Rev. A* **2013**, *87*, 013826.
- [23] Z.-J. Ying, M. Liu, H.-G. Luo, H.-Q. Lin, J. Q. You, *Phys. Rev. A* **2015**, *92*, 053823.
- [24] M. Liu, S. Chesi, Z.-J. Ying, X. Chen, H.-G. Luo, H.-Q. Lin, *Phys. Rev. Lett.* **2017**, *119*, 220601.
- [25] M.-J. Hwang, R. Puebla, M. B. Plenio, *Phys. Rev. Lett.* **2015**, *115*, 180404.
- [26] Z.-J. Ying, *Phys. Rev. A* **2021**, *103*, 063701.
- [27] Z.-J. Ying, *Adv. Quantum Technol.* **2022**, *5*, 2100088.
- [28] Z.-J. Ying, *Adv. Quantum Technol.* **2022**, *5*, 2100165.
- [29] Z.-J. Ying, L. Cong, X.-M. Sun, arXiv:1804.08128, **2018**; *J. Phys. A: Math. Theor.* **2020**, *53*, 345301.
- [30] H. P. Eckle, H. Johannesson, *J. Phys. A: Math. Theor.* **2017**, *50*, 294004.
- [31] Q.-T. Xie, S. Cui, J.-P. Cao, L. Amico, H. Fan, *Phys. Rev. X* **2014**, *4*, 021046.
- [32] S. Felicetti, D. Z. Rossatto, E. Rico, E. Solano, P. Forn-Díaz, *Phys. Rev. A* **2018**, *97*, 013851.
- [33] S. Felicetti, J. S. Pedernales, I. L. Egusquiza, G. Romero, L. Lamata, D. Braak, E. Solano, *Phys. Rev. A* **2015**, *92*, 033817.
- [34] L. Garbe, I. L. Egusquiza, E. Solano, C. Ciuti, T. Coudreau, P. Milman, S. Felicetti, *Phys. Rev. A* **2017**, *95*, 053854.
- [35] R. J. A. Rico, F. H. Maldonado-Villamizar, B. M. Rodríguez-Lara, *Phys. Rev. A* **2020**, *101*, 063825.
- [36] L. Garbe, M. Bina, A. Keller, M. G.A. Paris, S. Felicetti, *Phys. Rev. Lett.* **2020**, *124*, 120504.
- [37] L. Garbe, O. Abah, S. Felicetti, R. Puebla, arXiv:2112.11264, **2021**.
- [38] T. Ilias, D. Yang, S. F. Huelga, M. B. Plenio, *PRX Quantum* **2022**, *3*, 010354.
- [39] Z.-J. Ying, S. Felicetti, G. Liu, D. Braak, arXiv:2206.08410, **2022**.
- [40] A. Le Boité, M.-J. Hwang, H. Nha, M. B. Plenio, *Phys. Rev. A* **2016**, *94*, 033827.
- [41] A. Ridolfo, M. Leib, S. Savasta, M. J. Hartmann, *Phys. Rev. Lett.* **2012**, *109*, 193602.
- [42] E. K. Irish, A. D. Armour, arXiv:2203.17147, **2022**.
- [43] Z.-M. Li, D. Ferri, D. Tilbrook, M. T. Batchelor, *J. Phys. A: Math. Theor.* **2021**, *54*, 405201.
- [44] M. Liu, Z.-J. Ying, J.-H. An, H.-G. Luo, *New J. Phys.* **2015**, *17*, 043001.
- [45] L. Cong, X.-M. Sun, M. Liu, Z.-J. Ying, H.-G. Luo, *Phys. Rev. A* **2017**, *95*, 063803.
- [46] L. Cong, X.-M. Sun, M. Liu, Z.-J. Ying, H.-G. Luo, *Phys. Rev. A* **2019**, *99*, 013815.
- [47] K. K. W. Ma, *Phys. Rev. A* **2020**, *102*, 053709.
- [48] Q.-H. Chen, C. Wang, S. He, T. Liu, K.-L. Wang, *Phys. Rev. A* **2012**, *86*, 023822 (2012).
- [49] L. Duan, Y.-F. Xie, D. Braak, Q.-H. Chen, *J. Phys. A* **2016**, *49*, 464002.
- [50] Y.-Y. Zhang, *Phys. Rev. A* **2016**, *94*, 063824.
- [51] Z. Lü, C. Zhao, H. Zheng, *J. Phys. A: Math. Theor.* **2017**, *50*, 074002.
- [52] E. K. Irish, J. Gea-Banacloche, *Phys. Rev. B* **2014**, *89*, 085421.
- [53] J. Larson, E. K. Irish, *J. Phys. A: Math. Theor.* **2017**, *50*, 174002.
- [54] M. T. Batchelor, H.-Q. Zhou, *Phys. Rev. A* **2015**, *91*, 053808.
- [55] Q. Xie, H. Zhong, M. T. Batchelor, C. Lee, *J. Phys. A: Math. Theor.* **2017**, *50*, 113001.
- [56] S. Bera, S. Florens, H. U. Baranger, N. Roch, A. Nazir, A. W. Chin, *Phys. Rev. B* **2014**, *89*, 121108(R).
- [57] L. Yu, S. Zhu, Q. Liang, G. Chen, S. Jia, *Phys. Rev. A* **2012**, *86*, 015803.
- [58] T. Liu, M. Feng, W. L. Yang, J. H. Zou, L. Li, Y. X. Fan, K. L. Wang, *Phys. Rev. A* **2013**, *88*, 013820.
- [59] J. Peng, E. Rico, J. Zhong, E. Solano, I. L. Egusquiza *Phys. Rev. A* **2019**, *100*, 063820.
- [60] J. Casanova, R. Puebla, H. Moya-Cessa, M. B. Plenio, *npj Quantum Information* **2018**, *4*, 47.
- [61] D. Braak, *Symmetry* **2019**, *11*, 1259.
- [62] V. V. Mangazeev, M. T. Batchelor, V. V. Bazhanov, *J. Phys. A: Math. Theor.* **2021**, *54*, 12LT01.
- [63] Z.-M. Li, M. T. Batchelor, *Phys. Rev. A* **2021**, *103*, 023719.
- [64] C. Reyes-Bustos, D. Braak, M. Wakayama, *J. Phys. A: Math. Theor.* **2021**, *54*, 285202.
- [65] G. Romero, D. Ballester, Y. M. Wang, V. Scarani, E. Solano, *Phys. Rev. Lett.* **2012**, *108*, 120501.
- [66] R. Stassi, M. Cirio, F. Nori, *npj Quantum Information* **2020**, *6*, 67.
- [67] R. Stassi, F. Nori, *Phys. Rev. A* **2018**, *97*, 033823.
- [68] V. Macrì, F. Nori, A.F. Kockum, *Phys. Rev. A* **2018**, *98*, 062327.
- [69] A. Bermudez, M. A. Martin-Delgado, E. Solano, *Phys. Rev. A* **2007**, *76*, 041801(R).
- [70] M.-J. Hwang and M. B. Plenio, *Phys. Rev. Lett.* **2016**, *117*, 123602.
- [71] S. Sachdev, *Quantum phase transitions*, 2nd ed. Cambridge University Press, Cambridge, UK, **2011**.
- [72] Y. Wang, W.-L. You, M. Liu, Y.-L. Dong, H.-G. Luo, G. Romero, J. Q. You, *New J. Phys.* **2018**, *20*, 053061.
- [73] A. L. Grimsmo, S. Parkins, *Phys. Rev. A* **2013**, *87*, 033814.

- [74] A. L. Grimsmo, S. Parkins, *Phys. Rev. A* **2014**, *89*, 033802.
- [75] L. Cong, S. Felicetti, J. Casanova, L. Lamata, E. Solano, I. Arrazola, *Phys. Rev. A* **2020** *101*, 032350.
- [76] E. T. Jaynes, F. W. Cummings, *Proc. IEEE* **1963**, *51*, 89.
- [77] J. E. Mooij, T. P. Orlando, L. Levitov, L. Tian, C. H. van der Wal, S. Lloyd, *Science* **1999**, *285*, 1036.
- [78] Z.-C. Gu, X.-G. Wen, *Phys. Rev. B* **1990**, *80*, 155131.
- [79] Z.-X. Li, Y. Cao, X.R. Wang, P. Yan, *Phys. Rev. Applied* **2020**, *13*, 064058.
- [80] H. Zou, E. Zhao, X.-W. Guan, W. V. Liu, *Phys. Rev. Lett.* **2019**, *122*, 180401.
- [81] Y. Che, C. Gneiting, T. Liu, F. Nori, *Phys. Rev. B* **2020**, *102*, 134213.
- [82] F. Nagasawa, D. Frustaglia, H. Saarikoski, K. Richter, J. Nitta, *Nat. Commun.* **2013**, *4*, 2526.
- [83] Z.-J. Ying, P. Gentile, C. Ortix, M. Cuoco, *Phys. Rev. B* **2016**, *94*, 081406(R).
- [84] Z.-J. Ying, M. Cuoco, C. Ortix, P. Gentile, *Phys. Rev. B* **2017**, *96*, 100506(R).
- [85] Y.-J. Lin, K. Jiménez-García, I. B. Spielman, *Nature* **2011**, *471*, 83.
- [86] V. Galitski, Ian B. Spielman, *Nature* **2013**, *494*, 49.
- [87] G. Dresselhaus, *Phys. Rev.* **1955**, *100*, 580.
- [88] Y. A. Bychkov, E. I. Rashba, *J. Phys. C* **1984**, *17*, 6039.
- [89] Y. Li, L. P. Pitaevskii, S. Stringari, *Phys. Rev. Lett.* **2012**, *108*, 225301.
- [90] J. Larson and T. Mavrogordatos, *The Jaynes-Cummings Model and Its Descendants*, IOP, London, **2021**.
- [91] Y. Burda, *Ph.D. Thesis*, University of Toronto, Toronto, ON **2012**.
- [92] A. Amaricci, J. C. Budich, M. Capone, B. Trauzettel, G. Sangiovanni, *Phys. Rev. Lett.* **2015**, *114*, 185701.
- [93] C.-Z. Chen, J. Qi, D.-H. Xu, X.C. Xie, *Sci. China Phys. Mech. Astron.* **2021**, *64*, 127211.
- [94] Y.-F. Xie, X.-Y. Chen, X.-F. Dong, and Q.-H. Chen, *Phys. Rev. A* **2020**, *101*, 053803.
- [95] P. Bertet, I. Chiorescu, C. J. P. M. Harmans, J. E. Mooij, *arXiv:cond-mat/0507290*.
- [96] J. Q. You, Y. Nakamura, Franco Nori, *Phys. Rev. B* **2005**, *71*, 024532.
- [97] J. Casanova, G. Romero, I. Lizuain, J. J. García-Ripoll, E. Solano *Phys. Rev. Lett.* **2010** *105*, 263603.
- [98] J.-F. Huang, J.-Q. Liao, and L.-M. Kuang, *Phys. Rev. A* **2020**, *101*, 043835.